ple sclerosis (19, 20). In a previous study we reported that OSMRβ is expressed in adipose tissue macrophages (ATMs) and that OSM switches the phenotype of ATMs from the M1-type to the M2-type (21). In addition, disruption of OSMRβ gene in mice results in the development of mature-onset obesity and systemic insulin resistance under normal dietary conditions (21). However, the role of OSM signaling in the regulation of diet-induced obesity and related metabolic disorders remains unclear. In the present study we analyzed metabolic parameters in OSMR$\beta^{-/-}$ mice fed a high-fat diet (HFD) to investigate the role of OSM signaling in the development of obesity-induced metabolic disorders, including adipose tissue inflammation, insulin resistance, and hepatic steatosis.

EXPERIMENTAL PROCEDURES

Animals—Male C57BL/6J mice (8 weeks old) were purchased from Nihon SLC (Hamamatsu, Japan). Male +/+ (lean) and *ob/ob* mice (8 weeks old) were obtained from our breeding colony using heterozygous (*ob*/+) breeding pairs. The protocol used to generate OSMR$\beta^{-/-}$ mice has been described previously (22). OSMR$\beta^{+/+}$ wild-type (WT) and OSMR$\beta^{-/-}$ littermates were obtained from our breeding colony using heterozygous (+/−) breeding pairs. All mice were housed in specific pathogen-free facilities and light (12-h light/dark cycle)-, temperature (22–25 °C)-, and humidity (50–60% relative humidity)-controlled conditions. The mice were allowed free access to food and water. Until 8 weeks of age, all mice were fed a normal diet consisting of 13.3% calories from fat (MF; Oriental Yeast, Tokyo, Japan). At all times the experiments were performed under the control of the Animal Research Control Committee in accordance with the Guidelines for Animal Experiments of Wakayama Medical University, Japanese Government Notification on Feeding and Safekeeping of Animals (no. 6) and National Institutes of Health Guide for the Care and Use of Laboratory Animals (NIH publication no. 80–23, revised 1978). All efforts were made to minimize the number of animals used and their suffering.

HFD—Diet-induced obese (DIO) mice were generated by placing male C57BL/6J mice on an HFD consisting of 56.7% of calories from fat (High Fat Diet 32; CLEA Japan, Tokyo, Japan) beginning at 8 weeks of age for 8 weeks. OSMR$\beta^{-/-}$ mice and their littermates were placed on the HFD starting at 8 weeks of age and fed in individual cages for 2, 4, or 8 weeks.

Pair-feeding on the HFD—Pair-feeding study was performed with some modifications as described by Racioppi *et al.* (23). WT and OSMR$\beta^{-/-}$ mice at 8 weeks of age were housed in individual cages. The amount of food intake for the WT mice fed *ad libitum* and OSMR$\beta^{-/-}$ mice fed *ad libitum* was monitored daily for the duration of the experiment. As OSMR$\beta^{-/-}$ mice fed *ad libitum* would eat more food than WT mice fed *ad libitum*, OSMR$\beta^{-/-}$ mice received the average amount of food consumed by the WT mice. All mice had free access to water. The food was provided to mice every day at 18:00, 2 h before the dark period began. Pair-feeding was carried out for 8 weeks. Body weights were recorded once a week throughout the experiment.

Injection of OSM in ob/ob Mice—Injection of OSM was performed as described previously (21). Briefly, *ob/ob* mice were administrated intraperitoneally with either vehicle or recombinant mouse OSM (12.5 ng/g of body weight; R & D Systems, Minneapolis, MN) twice a day (10:00 and 18:00 h) for 1 week.

Intraportal Administration of OSM in ob/ob Mice—To investigate the direct effects of OSM on the liver of obese mice, *ob/ob* mice were deeply anesthetized with isoflurane and administrated intraportally with either vehicle or recombinant mouse OSM (12.5 ng/g of body weight). After 15, 30, 60, or 120 min of administration, the livers were excised, and the tissue lysates were prepared as described below.

Isolation of the Adipocyte Fraction and Stromal Vascular Fraction (SVF)—Isolation of the adipocyte fraction and SVF was performed as previously described (21). The mice were deeply anesthetized with diethyl ether, and the epididymal adipose tissue was quickly removed. The adipose tissue was minced into fine pieces and digested with collagenase type 2 (Sigma) dissolved in PBS supplemented with 2% FCS at 37 °C for 20 min. Next, the samples were passed through a nylon mesh (100-μm pore size; BD Biosciences) and fractioned by brief centrifugation (1200 rpm) at room temperature (RT) for 5 min. Floating cells and pellets were collected as the adipocyte fraction and SVF, respectively. The cells in the SVF were incubated with ammonium chloride buffer (PharmLyse; BD Biosciences) to lyse the erythrocytes.

Flow Cytometry—Flow cytometry was performed as previously described (21). The cells in the SVF were incubated with anti-CD16/CD32 antibodies (1:100, BD Biosciences) to block Fc binding at 4 °C for 20 min. The cells were then incubated with the following primary antibodies at 4 °C for 30 min: fluorescein isothiocyanate-conjugated anti-F4/80 antibody (eBiosciences), phycoerythrin-conjugated anti-CD11c antibody (eBiosciences), and Alexa Fluor 647-conjugated anti-CD206 antibody (AbD Serotec). To detect OSMRβ in the SVF, cells were incubated with goat anti-OSMRβ antibody (diluted at 1:5, R&D Systems) at 4 °C for 30 min. Then, the cells were incubated with phycoerythrin-conjugated donkey anti-goat IgG (diluted at 1: 20, R&D Systems). The stained cells were analyzed using the C6 flow cytometer (BD Biosciences) or the FACSCalibur flow cytometer (BD Biosciences). The stained cells were analyzed using the C6 flow cytometer (Accuri Cytometers). Dead cells were removed from the analysis using propidium iodide staining. The flow cytometry results were analyzed using the FlowJo (Tree Star) software suite. The events were first gated based on a forward scatter plot *versus* propidium iodide to identify individual live cells. The plot of a forward- *versus* side-scatter pattern was used as the second gate to gate out aggregates and debris. The cells gated on the F4/80-positive population were then analyzed for CD11c, CD206, and OSMRβ. Single color controls were used to set the compensation and gates.

Insulin Signaling Analysis—An insulin signaling analysis was performed as previously described (21). To evaluate insulin signaling, mice fasted for 24 h were intraperitoneally injected with human insulin (10 milliunits/g of body weight). Ten minutes later epididymal adipose tissue, gastrocnemius muscle, and liver were excised and frozen in liquid nitrogen. Tissue lysates were prepared as described below.

Western Blot Analysis—Western blot analysis was performed with some modifications, as previously described (24). Tissue lysates were prepared using radioimmune precipitation assay buffer (Upstate Biotechnology) containing protease inhibitor mixture (Upstate Biotechnology), 1 mM orthovanadate, 1 mM sodium fluoride, and 1 mM phenylmethylsulfonyl fluoride. The protein concentrations in the lysates were determined using a BCA Protein Assay kit (Pierce). Twenty micrograms of protein obtained from the samples was separated by sodium dodecyl sulfate-polyacrylamide gel electrophoresis (SDS-PAGE) and transferred to PVDF membranes (GE Healthcare). The blotted membranes were incubated with goat anti-OSMRβ antibody (diluted 1:1000, R&D Systems), rabbit anti-phosphorylated Akt antibody (diluted at 1:1000, Cell Signaling Technology), rabbit anti-phosphorylated FOXO1 antibody (diluted at 1:1000, Cell Signaling Technology), rabbit anti-phosphorylated p70 S6 kinase (S6K) antibody (diluted at 1:1000, Cell Signaling Technology), and rabbit anti-phosphorylated STAT3 antibody (diluted at 1:1000, Cell Signaling Technology). The membranes were then incubated with HRP-conjugated donkey anti-goat (diluted at 1:10,000, Jackson ImmunoResearch) or donkey anti-rabbit (diluted at 1:4,000, GE Healthcare) antibodies. Labeled proteins were detected with chemiluminescence using ECL detection reagent (GE Healthcare) according to the manufacturer's instructions. The membranes were exposed to hyperfilm ECL (GE Healthcare) for an appropriate period. The blotted membranes were stripped in 0.25 M of glycine, pH 2.5, at RT for 10 min and incubated with rat anti-tubulin antibody (diluted at 1:500; Abcam), rabbit anti-FOXO1 antibody (diluted at 1:1000, Cell Signaling Technology), rabbit anti-S6K antibody (diluted at 1:1000, Cell Signaling Technology), and rabbit anti-STAT3 antibody (diluted at 1:1000, Cell Signaling Technology) at 4 °C for 16 h followed by incubation with HRP-conjugated donkey anti-rat (diluted at 1:4000, Jackson ImmunoResearch) or donkey anti-rabbit antibodies (diluted at 1:4000, Jackson ImmunoResearch) at RT for 1 h.

Immunohistochemistry—Immunofluorescence staining was performed with some modifications as previously described (25). Briefly, the mice were deeply anesthetized with diethyl ether, and the epididymal adipose tissue was quickly removed. The adipose tissue was then fixed with 1% paraformaldehyde in PBS at 4 °C for 1 h followed by preincubation in 5% normal donkey serum at RT for 1 h. The adipose tissue was subsequently incubated with goat anti-OSMRβ antibody (diluted at 1:400), rat anti-F4/80 antibody (diluted at 1:1000; AbD Serotec), and rabbit anti-caveolin-1 antibody (diluted at 1:400; BD Biosciences). The adipose tissue was incubated with Cy2-conjugated, Cy3-conjugated, or biotinylated secondary antibodies (diluted at 1:800; Jackson ImmunoResearch) at RT for 1 h. The adipose tissue was then incubated with 7-amino-4-methylcoumarin-3-acetic acid-conjugated streptavidin (diluted at 1:500; Jackson ImmunoResearch) at RT for 30 min and mounted in mounting media (90% glycerol and 10% PBS) on the chambered slide. Immunofluorescence images were acquired using a confocal laser scanning microscope (LSM700; Carl Zeiss).

Immunohistochemical analysis of pancreas was performed as previously described (21). Briefly, 6-μm-thick frozen sections were treated with normal donkey serum and incubated with rabbit anti-insulin antibody (diluted at 1:400; Abcam). Then they were incubated with biotinylated donkey anti-rabbit IgG antibody (diluted at 1:800; Jackson ImmunoResearch) followed by the incubation with HRP-conjugated streptoavidin (DAKO, Carpinteria, CA). Thereafter, the peroxidase reaction was developed with 0.05% diaminobenzidine tetrahydrochloride (Sigma) and 0.01% H_2O_2. Eosin Y (Muto Pure Chemical, Tokyo, Japan) was used for counterstaining. Images were acquired by using a BIOREVO BZ-9000 microscope (KEYENCE, Osaka, Japan). To evaluate the area of β-cell in pancreas, every 20th section was selected from a series of consecutive pancreatic sections, and 12 sections per mouse were used for the analysis. For each section, the cells were considered to be positive for insulin if the cell bodies were stained brown. The area of β-cells and pancreas was quantified using Image J analysis software (Version 1.46r, Scion, Frederick, MD).

The following controls were performed: (i) incubation with protein A-purified goat or rabbit IgG instead of primary antibody; (ii) incubation without the primary antibody or without primary and secondary antibodies. All controls revealed no labeling (data not shown).

Measurement of Blood Glucose and Serum Insulin—Measurements of the blood glucose and serum insulin levels were obtained as previously described (21). The mice were fasted for 4 h to remove the effects of food intake on glucose metabolism, and blood was removed from the tail vein at 18:00 h. In the fasting experiments the mice were fasted overnight with free access to water. Serum was then immediately collected and stored at −20 °C. The blood glucose levels were measured with a glucose measurement device (Glucocard GT-1640, Arkray). The serum insulin concentrations were determined using kits from Morinaga.

Intraperitoneal Glucose Tolerance Tests (ipGTT) and Insulin Tolerance Tests (ITT)—ipGTT and ITT were performed as previously described (21). For the ipGTT, the mice were fasted for overnight, after which they received an intraperitoneal injection of D-glucose. Blood samples were collected from the tail vein before and at 15, 30, 60, and 120 min after the injection of D-glucose. For the ITT, the mice were fasted for 4 h, after which they received an intraperitoneal injection of human insulin. Blood samples were collected from the tail vein before and at 15, 30, 60, and 120 min after the injection of insulin.

ELISA—The concentrations of TNF-α, IL-10, and adiponectin were measured with ELISA kits (R & D Systems) according to the manufacturer's instructions. The serum leptin concentration was determined using an ELISA kit from Morinaga. The serum amyloid A concentration was measured with an ELISA kit from Invitrogen.

Measurement of the Lipid Content in the Serum and Liver—The serum levels of triglycerides, total cholesterol, and free fatty acids were measured at Nagahama Life Science Laboratory using lipid assay kits (Triglyceride E-Test Wako, Total Cholesterol E-Test Wako, and NEFA C-Test Wako, Wako Pure Chemical Industries) according to the manufacturer's instructions. The content of triglycerides and total cholesterol in the liver was analyzed at Skylight Biotech (Akita, Japan).

As described previously (21), the mice were fasted for 4 h to remove the effects of food intake on lipid metabolism, and liver

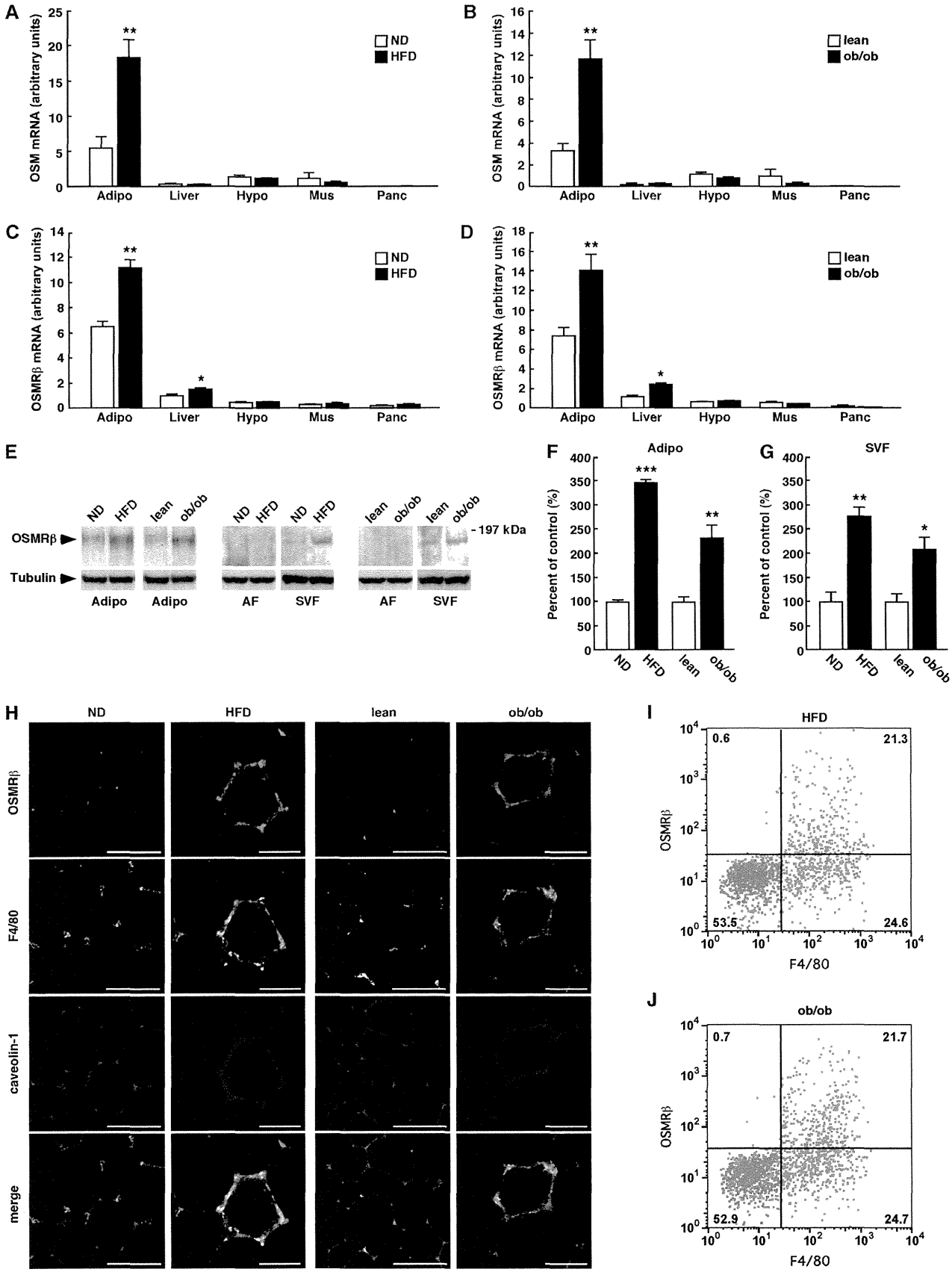
A
OSM mRNA (arbitrary units)
ND
HFD
Adipo
Liver
Hypo
Mus
Panc
B
OSM mRNA (arbitrary units)
lean
ob/ob
C
OSMRβ mRNA (arbitrary units)
D
OSMRβ mRNA (arbitrary units)
E
OSMRβ
Tubulin
- 197 kDa
ND
HFD
lean
ob/ob
Adipo
AF
SVF
F
Adipo
Percent of control (%)
G
SVF
H
ND
HFD
lean
ob/ob
OSMRβ
F4/80
caveolin-1
merge
I
HFD
0.6
21.3
53.5
24.6
F4/80
J
ob/ob
0.7
21.7
52.9
24.7

was dissected at 15:00 h. In the fasting experiments the mice were fasted for overnight with free access to water. Lipids were extracted from the liver according to the Folch method (26). The frozen liver tissues were homogenized, and triglycerides and total cholesterol were extracted from the homogenate with chloroform/methanol (2:1, v/v), dried, and resuspended in 2-propanol. The amounts of triglycerides and total cholesterol in the extract were measured using lipid assay kits (Cholestest TG and Cholestest CHO, Sekisui Medical).

Quantitative Real-time PCR—Quantitative real-time PCR was performed with some modifications, as previously described (25). Briefly, total RNA extracted from epididymal adipose tissue, SVF, liver, hypothalamus, skeletal muscle, and pancreas was prepared using TRI reagent (Molecular Research Center). The cDNA from the total RNA was synthesized with TaqMan Reverse Transcription Reagents (Applied Biosystems). The following TaqMan Gene Expression Assays (Applied Biosystems) were used: OSM (Mm01193966_m1), OSMRβ (Mm00495424_m1), insulin (P/N4323969), TNF-α (Mm00443258_m1), IL-1β (Mm00434228_m1), interferon-γ (IFN-γ) (Mm00801778_m1), monocyte chemoattractant protein-1 (MCP-1) (Mm00441242_m1), C-C chemokine receptor 2 (CCR2) (Mm00438270_m1), toll-like receptor 4 (TLR4) (Mm00445273_m1), IL-6 (Mm00446190_m1), IL-10 (Mm00439616_m1), IL-13 (Mm00434204_m1), adiponectin (Mm00456425_m1), macrophage galactose-type C-type lectin 1 (MGL1) (Mm00546124_m1), MGL2 (Mm00460844_m1), fatty-acid synthase (FAS) (Mm00662319_m1), stearoyl CoA desaturase-1 (SCD-1) (Mm00772290_m1), sterol regulatory-element binding transcription factor-1 (SREBF-1) (Mm00550338_m1), ACSL3 (Mm01255804_m1), ACSL5 (Mm01261083_m1), and 18S (Hs99999901_s1). Quantitative real-time PCR of each gene was performed using Rotor Gene Q (Qiagen) and Rotor Gene Probe PCR kits (Qiagen). The PCR amplification protocol was as follows: 95 °C for 10 min followed by 40 cycles of 95 °C for 10 s and 60 °C for 45 s. The relative abundance of transcripts was normalized according to the expression of 18 S mRNA and analyzed using the ΔΔCT method.

Statistical Analysis—The results are presented as the mean ± S.E. Statistically significant differences between groups were analyzed using Student's *t* test or an analysis of variance followed by the post-hoc Bonferroni test. The criterion for statistical significance was a p value of < 0.05.

RESULTS

Expression of OSMRβ in the Adipose Tissue of the Obese Mice—We previously reported that OSMRβ is expressed in adipose tissue, especially in the ATMs of C57BL/6J mice under normal dietary conditions (21). We first investigated the expression levels of OSM and OSMRβ in various tissues of two types of obese model mice, DIO mice and genetically obese *ob/ob* mice. In non-obese mice, both OSM and OSMRβ were abundantly expressed in the adipose tissue (Fig. 1, *A–D*). The expression of OSM only increased in the adipose tissues of both types of obese model mice (Fig. 1, *A* and *B*). In contrast, the OSMRβ expression was increased in the adipose tissue and liver but not in the hypothalamus, skeletal muscle, and pancreas in the obese mice (Fig. 1, *C* and *D*). In the adipose tissue, the expression of OSMRβ was predominantly increased in the SVF in DIO and *ob/ob* mice compared with that observed in the respective control mice (Fig. 1, *E–G*). However, OSMRβ was rarely detected in the adipocyte fraction of all mice examined (Fig. 1*E*). Immunofluorescence staining revealed that OSMRβ was expressed in F4/80-positive macrophages in the adipose tissue of the DIO and *ob/ob* mice and the respective control mice (Fig. 1*H*). However, the intensity of staining for OSMRβ in macrophages and the number of OSMRβ-positive macrophages were increased in the adipose tissue in the DIO and *ob/ob* mice compared with those observed in the respective control mice (Fig. 1*H*). Flow cytometric analysis revealed that OSMRβ was exclusively expressed in F4/80-positive macrophages in the adipose tissue of both the DIO (97.0 ± 1.1%; Fig. 1*I*) and *ob/ob* mice (96.7 ± 0.3%; Fig. 1*J*). In addition, almost half of F4/80-positive macrophages was OSMRβ-positive in the adipose tissue of the DIO (45.0 ± 1.1%; Fig. 1*I*) and *ob/ob* mice (43.8 ± 1.7%; Fig. 1*J*).

OSMRβ$^{-/-}$ Mice Develop Obesity and Insulin Resistance under HFD Conditions—To investigate the roles of OSM signaling in the development of obesity-induced metabolic disorders, we fed 8-week-old OSMRβ$^{-/-}$ mice and WT littermates an HFD for 8 weeks. As the amount of food intake and the food intake per body weights were increased in OSMRβ$^{-/-}$ mice compared with that observed in WT mice under HFD conditions (Fig. 2, *D* and *E*), we conducted a pair-feeding study to investigate the effects of food intake on metabolic parameters in OSMRβ$^{-/-}$ mice. Remarkably, OSMRβ$^{-/-}$ mice began to gain more weight than WT mice at 4 weeks on the HFD and remained heavier until 8 weeks on the HFD (Fig. 2, *A* and *B*). In OSMRβ$^{-/-}$ mice pair-fed with WT mice, designated OSMRβ$^{-/-}$(PF) mice, the body weight values were similar to those in WT mice (Fig. 2, *A* and *B*). The weights of the adipose tissues (epididymal and subcutaneous) of OSMRβ$^{-/-}$ mice were heavier than those of WT and OSMRβ$^{-/-}$(PF) mice at 8 weeks on the HFD (Fig. 2*C*). Consistent with these data, the serum concentration of leptin in OSMRβ$^{-/-}$ mice was higher

FIGURE 1. **The expressions of OSM and OSMRβ in various tissues of non-obese and obese mice.** *A* and *B*, the mRNA expressions of OSM in the adipose tissue, liver, hypothalamus, skeletal muscle, and pancreas in the WT mice fed a normal diet (*ND*) or a HFD (*A*) and the lean and *ob/ob* mice (*B*) ($n = 6$). *C* and *D*, the mRNA expressions of OSMRβ in the adipose tissue, liver, hypothalamus, skeletal muscle, and pancreas in the WT mice fed a ND or an HFD (*C*) and the WT and *ob/ob* mice (*D*) ($n = 6$). *E*, Western blot analysis of OSMRβ in the adipose tissues of the non-obese and obese mice. The apparent molecular masses are indicated on the *right*. Bands corresponding to OSMRβ were detected at 180 kDa. *F* and *G*, a quantitative analysis of the protein expression of OSMRβ in the entire adipose tissue specimen (*F*) and SVF (*G*) ($n = 6$). *H*, immunofluorescence staining for OSMRβ (*red*) with F4/80 (*green*) and caveolin-1 (*blue*) in the adipose tissues of the obese mice and the respective controls. *Scale bar* = 100 μm. *I* and *J*, the expression of OSMRβ and F4/80 in SVF cells analyzed by flow cytometry. Isolated SVF cells from the adipose tissue of DIO (*I*) and *ob/ob* mice (*J*) were stained with antibodies against F4/80 and OSMRβ (*blue dots*). *Red dots* show the data with their control antibodies ($n = 4$). *ND*, C57BL/6J mice fed a normal diet at 16 weeks old; *HFD*, C57BL/6J mice fed an HFD for 8 weeks started at 8 weeks old; *lean*, control for *ob/ob* mice at 8 weeks old; *ob/ob*, *ob/ob* mice at 8 weeks old; *Adipo*, adipose tissue; *AF*, adipocyte fraction; *Hypo*, hypothalamus; *Mus*, skeletal muscle; *Panc*, pancreas. The data represent the mean ± S.E. *, $p < 0.05$; **, $p < 0.01$; ***, $p < 0.005$ normal diet (*ND*) *versus* HFD or lean *versus ob/ob*, Student's *t* test.

than that observed in WT and OSMRβ$^{-/-}$(PF) mice (Table 1). However, the serum concentration of adiponectin did not differ between the three groups (Table 1).

The blood glucose concentration in OSMRβ$^{-/-}$ and OSMRβ$^{-/-}$(PF) mice began to increase compared with those observed in WT mice after 6 weeks on the HFD (Fig. 2*F*), whereas the serum insulin concentration in OSMRβ$^{-/-}$ and OSMRβ$^{-/-}$(PF) mice began to increase after 1 week on the HFD and continued to increase for 8 weeks (Fig. 2*G*). After 8 weeks on the HFD, the concentrations of blood glucose and serum insulin were increased in OSMRβ$^{-/-}$ and OSMRβ$^{-/-}$(PF) mice compared with those observed in WT mice under both fed and fasted states (Table 1). There were no significant differences in the concentrations of blood glucose and serum insulin between

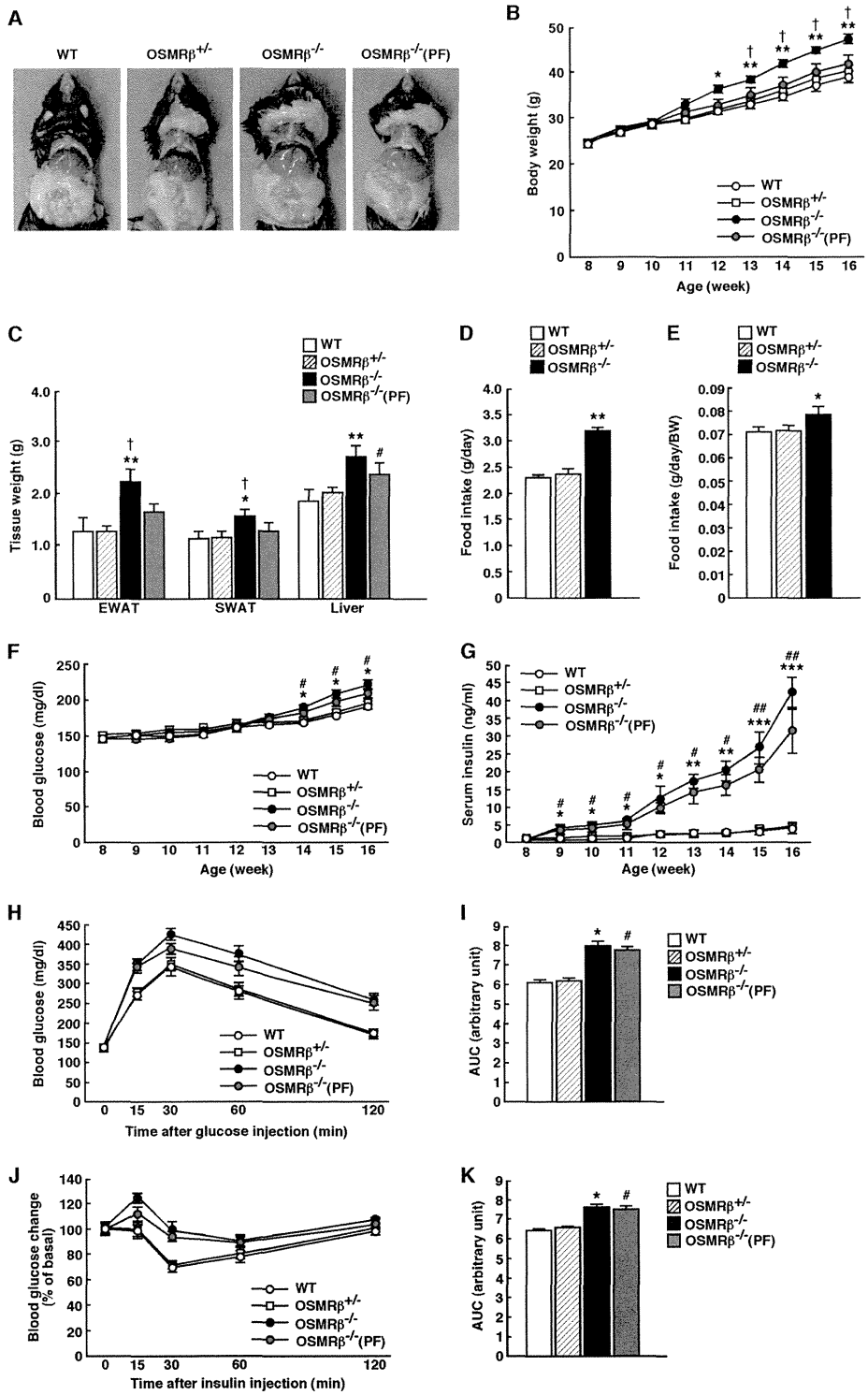

TABLE 1

Various metabolic parameters in the serum of WT and OSMRβ$^{-/-}$ mice under HFD conditions (n = 6–8)

In the fed states, mice were fasted for 4 h before the experiments to eliminate the feeding effect on lipid metabolism. In the fasted states, mice were fasted for overnight before the experiments. The data represent the mean ± S.E.

Serum concentration	WT	OSMRβ$^{-/-}$	OSMRβ$^{-/-}$(PF)
Leptin (ng/ml)	19.0 ± 2.2	25.7 ± 1.3[a,b]	22.6 ± 1.8
Serum amyloid A (ng/ml)	26.9 ± 7.0	69.3 ± 15.8[a]	46.8 ± 9.1[c]
TNF-α (pg/ml)	5.80 ± 0.32	6.41 ± 0.23[a]	6.13 ± 0.18
IL-10 (pg/ml)	11.7 ± 1.1	14.4 ± 0.5[a]	12.9 ± 1.5
Adiponectin (μg/ml)	22.8 ± 0.1	22.9 ± 0.8	22.6 ± 1.8
Glucose (fed) (mg/dl)	163.7 ± 17.2	235.3 ± 8.3[d]	203.8 ± 16.9[c]
Glucose (fasted) (mg/dl)	119.3 ± 3.5	126.3 ± 1.9[a]	125.8 ± 3.3[c]
Insulin (fed) (ng/ml)	4.14 ± 1.42	42.0 ± 4.5[a]	36.4 ± 6.2[c]
Insulin (fasted) (ng/ml)	1.73 ± 2.81	20.0 ± 3.8[a]	16.3 ± 8.2[c]
Total cholesterol (fed) (mg/dl)	153.8 ± 11.6	200.3 ± 17.3[a]	186.2 ± 19.6[c]
Total cholesterol (fasted) (mg/dl)	70.0 ± 6.3	104.8 ± 7.7[a]	Not tested
Triglyceride (fed) (mg/dl)	147.0 ± 12.6	175.5 ± 13.6[a]	164.0 ± 6.4[c]
Triglyceride (fasted) (mg/dl)	22.0 ± 1.9	36.0 ± 6.6[a]	Not tested
Free fatty acid (fed) (mmol/liter)	1.76 ± 0.09	1.90 ± 0.13	1.90 ± 0.08
Free fatty acid (fasted) (mmol/liter)	0.75 ± 0.04	0.83 ± 0.05	Not tested

[a] $p < 0.05$ WT *versus* OSMRβ$^{-/-}$ mice, Student's t test.
[b] $p < 0.05$ OSMRβ$^{-/-}$ *versus* OSMRβ$^{-/-}$ (PF) mice, Student's t test.
[c] $p < 0.05$ WT *versus* OSMRβ$^{-/-}$ (PF) mice, Student's t test.
[d] $p < 0.01$ WT *versus* OSMRβ$^{-/-}$ mice, Student's t test.

OSMRβ$^{-/-}$ and OSMRβ$^{-/-}$(PF) mice (Table 1). The ipGTTs and ITTs demonstrated that glucose tolerance and insulin sensitivity were reduced in OSMRβ$^{-/-}$ mice compared with those observed in WT mice at 8 weeks on the HFD, as measured by the area under the curves (AUCs) of blood glucose on the ipGTTs and ITTs (Fig. 2, *H–K*). There were no significant differences in the AUCs of blood glucose between OSMRβ$^{-/-}$ and OSMRβ$^{-/-}$(PF) mice (Fig. 2, *I* and *K*). There were no significant differences in the body weights, tissue weights, food intake, blood glucose, and serum insulin between WT and heterozygous OSMRβ-deficient mice (OSMRβ$^{+/-}$ mice) under HFD conditions (Fig. 2).

Similar to the data obtained from the male mice, the body weights, tissue weights, and the level of food intake were also increased in the female OSMRβ$^{-/-}$ mice fed the HFD compared with those observed in female WT mice fed the HFD (Fig. 3, *A–D*). In addition, the female OSMRβ$^{-/-}$ mice fed the HFD exhibited more severe glucose intolerance than female WT mice fed the HFD, as measured on the ipGTTs (Fig. 3, *E* and *F*).

OSMRβ$^{-/-}$ Mice Exhibit Severe Hepatic Steatosis under HFD Conditions—The liver weight in OSMRβ$^{-/-}$ mice, which was not significantly different from that in OSMRβ$^{-/-}$(PF) mice, was heavier than that in WT mice (Fig. 2*C*). To detect intracellular lipid droplets and glycogen granules in the liver, we performed Oil Red O and periodic acid-Schiff (PAS) staining, respectively. The Oil Red O staining revealed that lipid accumulation was augmented in the livers of OSMRβ$^{-/-}$ and OSMRβ$^{-/-}$(PF) mice compared with that observed in WT mice (Fig. 4*A*). In contrast, the PAS staining showed that there were fewer glycogen granules in the hepatocytes of OSMRβ$^{-/-}$ and OSMRβ$^{-/-}$(PF) mice compared with those observed in WT mice (Fig. 4*A*). Consistent with these data, the serum concentrations of total cholesterol and triglyceride were increased in OSMRβ$^{-/-}$ and OSMRβ$^{-/-}$(PF) mice compared with those observed in WT mice in both fed and fasted states (Table 1). There was a tendency for the serum concentration of free fatty acids to be increased in OSMRβ$^{-/-}$ and OSMRβ$^{-/-}$(PF) mice compared with that observed in WT mice in both fed and fasted states; however, their differences were not statistically significant (Table 1). In addition, the total cholesterol and triglyceride levels in the livers of OSMRβ$^{-/-}$ and OSMRβ$^{-/-}$(PF) mice were higher than those observed in WT mice (Fig. 4, *B* and *C*). To provide insight into the cause of the increased lipid accumulation observed in the livers of OSMRβ$^{-/-}$ and OSMRβ$^{-/-}$(PF) mice, we investigated the expression levels of genes related to fatty acid synthesis in the liver. The expression levels of FAS, SCD-1, and SREBF-1 were increased in the livers of OSMRβ$^{-/-}$ and OSMRβ$^{-/-}$(PF) mice compared with those observed in the liver of WT mice (Fig. 4*D*). In addition, phosphorylation of S6K, which increases the activity of SREBF-1 (27), was up-regulated in the liver of OSMRβ$^{-/-}$ and OSMRβ$^{-/-}$(PF) mice (Fig. 4, *E* and *F*). Thus, severe hepatic steatosis concomitant with enhanced S6K activation and increased lipogenic gene expression was observed in the liver of OSMRβ$^{-/-}$ mice.

Impaired Insulin Signaling in OSMRβ$^{-/-}$ Mice under HFD Conditions—To evaluate insulin signaling pathways in adipose tissue, skeletal muscle, and liver, we investigated the phosphor-

FIGURE 2. **Body weight and glucose metabolism in WT and OSMRβ$^{-/-}$ mice under HFD conditions.** The mice (8 weeks old) were fed an HFD for 8 weeks. *A*, representative images of WT mice, OSMRβ$^{+/-}$ mice, OSMRβ$^{-/-}$ mice, and OSMRβ$^{-/-}$ mice pair-fed with WT mice (*PF*). *B*, the body weights of WT, OSMRβ$^{+/-}$, OSMRβ$^{-/-}$, and OSMRβ$^{-/-}$(PF) mice (n = 6–11). *C*, the tissue weights in WT, OSMRβ$^{+/-}$, OSMRβ$^{-/-}$, and OSMRβ$^{-/-}$(PF) mice at 8 weeks on the HFD (n = 6–11). *EWAT*, epididymal white adipose tissue; *SWAT*, subcutaneous white adipose tissue. *D*, the amount of food intake in WT, OSMRβ$^{+/-}$, OSMRβ$^{-/-}$, and OSMRβ$^{-/-}$(PF) mice at 8 weeks on the HFD (n = 6–11). *E*, the amount of food intake per body weights in WT, OSMRβ$^{+/-}$, OSMRβ$^{-/-}$, and OSMRβ$^{-/-}$(PF) mice at 8 weeks on the HFD (n = 6–11). *F* and *G*, the blood glucose (*F*) and serum insulin (*G*) levels in WT, OSMRβ$^{+/-}$, OSMRβ$^{-/-}$, and OSMRβ$^{-/-}$(PF) mice in the fed state (n = 6). In the fed states, mice were fasted for 4 h before the experiments to eliminate the feeding effects on glucose metabolism. *H–K*, the results of the ipGTTs (*H*) and ITTs (*J*) in WT, OSMRβ$^{+/-}$, OSMRβ$^{-/-}$, and OSMRβ$^{-/-}$(PF) mice at 8 weeks on the HFD (n = 6). For ipGTTs, mice were fasted for 16 h and intraperitoneally injected with D-glucose (1 g/kg of body weight). For ITTs, mice were fasted for 4 h and intraperitoneally injected with insulin (1 unit/kg of body weight). The AUC for blood glucose on the ipGTTs (*I*) and ITTs (*K*) is shown. The data represent the mean ± S.E. *, $p < 0.05$; **, $p < 0.01$; ***, $p < 0.005$ WT *versus* OSMRβ$^{-/-}$ mice; #, $p < 0.05$; ##, $p < 0.01$ WT *versus* OSMRβ$^{-/-}$(PF) mice; †, $p < 0.05$ OSMRβ$^{-/-}$ *versus* OSMRβ$^{-/-}$(PF) mice, analysis of variance followed by the post-hoc Bonferroni test (*B*, *F*, and *G*); Student's t test (*C*, *D*, *E*, *I*, and *K*).

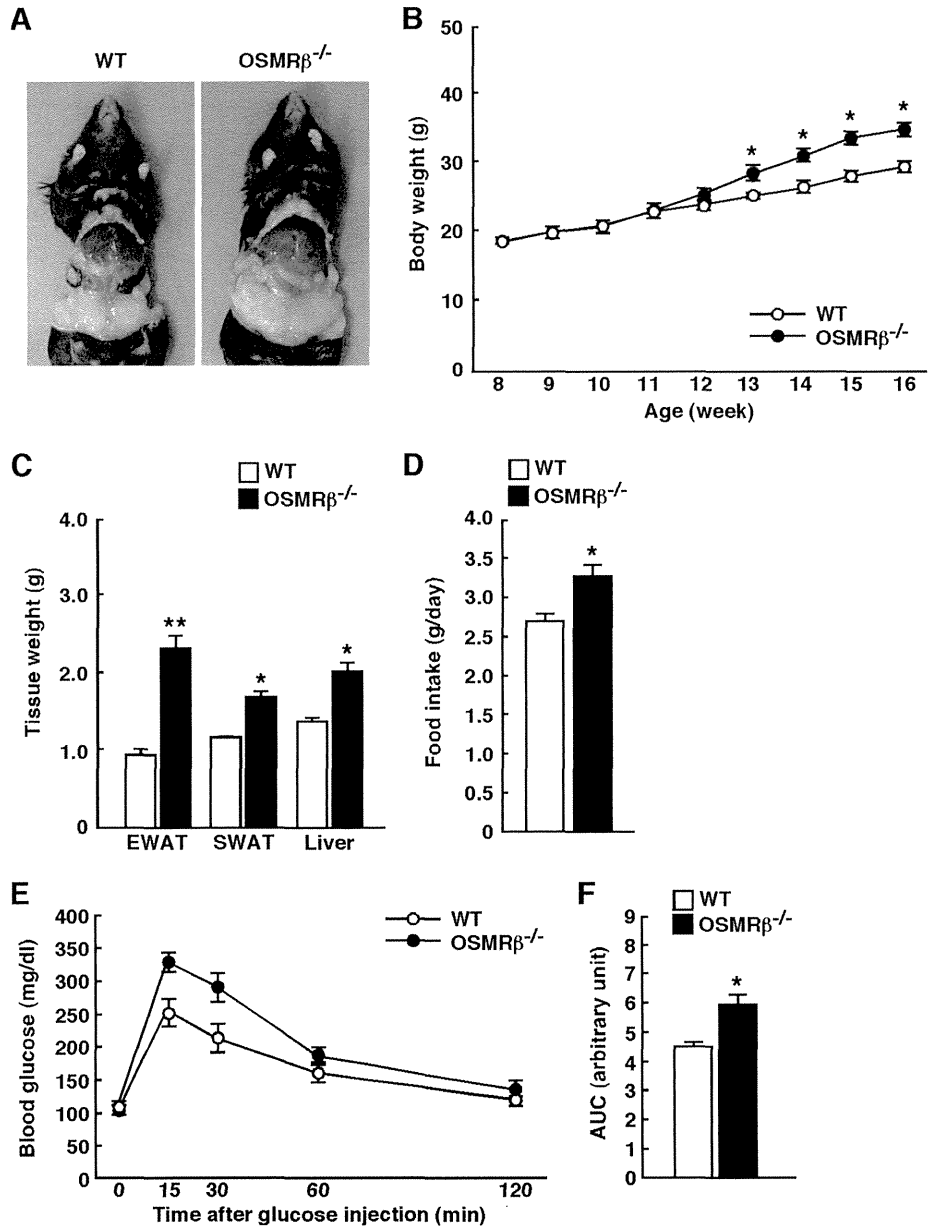

FIGURE 3. **Body weights and glucose metabolism in the female WT and OSMR$\beta^{-/-}$ mice under HFD conditions.** The mice (8 weeks old) were fed an HFD for 8 weeks. *A*, representative images of the female WT and OSMR$\beta^{-/-}$ mice. *B*, the body weights of the female WT and OSMR$\beta^{-/-}$ mice ($n = 6$). *C*, the tissue weights in the female WT and OSMR$\beta^{-/-}$ mice at 8 weeks on the HFD ($n = 6$). *EWAT*, epididymal white adipose tissue; *SWAT*, subcutaneous white adipose tissue. *D*, the amount of food intake in the female WT and OSMR$\beta^{-/-}$ mice ($n = 6$). *E* and *F*, the results of the ipGTTs in the female WT and OSMR$\beta^{-/-}$ mice at 8 weeks on the HFD ($n = 6$). For ipGTTs, mice were fasted for 16 h and intraperitoneally injected with D-glucose (1 g/kg of body weight). The AUC for glucose on the ipGTTs (*F*) is shown. The data represent the mean ± S.E. *, $p < 0.05$; **, $p < 0.01$ WT *versus* OSMR$\beta^{-/-}$ mice, analysis of variance followed by the post-hoc Bonferroni test (*B*); Student's *t* test (*C*, *D*, and *F*).

ylation level of Akt induced by the stimulation with insulin in each tissue. Without the stimulation with insulin, phosphorylation of Akt was hardly observed in the adipose tissue, skeletal muscle, and liver of WT, OSMR$\beta^{-/-}$, and OSMR$\beta^{-/-}$(PF) mice in the fasted states (data not shown). After the stimulation with insulin, Akt was phosphorylated in the adipose tissue, skeletal muscle, and liver of these mice (Fig. 5*A*). However, the level of insulin-induced Akt phosphorylation was decreased in the adipose tissue, skeletal muscle, and liver of OSMR$\beta^{-/-}$ and OSMR$\beta^{-/-}$(PF) mice compared with that observed in WT mice (Fig. 5*B*).

Next, we examined the phosphorylation level of FOXO1 and S6K, which are important for the suppression of gluconeogenesis (28) and the activation of lipogenesis (29), respectively, in the liver. Without the stimulation with insulin, phosphorylation of FOXO1 and S6K was hardly observed in the liver of WT, OSMR$\beta^{-/-}$, and OSMR$\beta^{-/-}$(PF) mice in the fasted state (data not shown). After the stimulation with insulin, FOXO1 and S6K were phosphorylated in the livers of these mice (Fig. 5, *C–F*). In addition, phosphorylation level of FOXO1 was decreased in the liver of OSMR$\beta^{-/-}$ and OSMR$\beta^{-/-}$(PF) mice compared with that observed in WT mice (Fig. 5*D*). In contrast, phosphoryla-

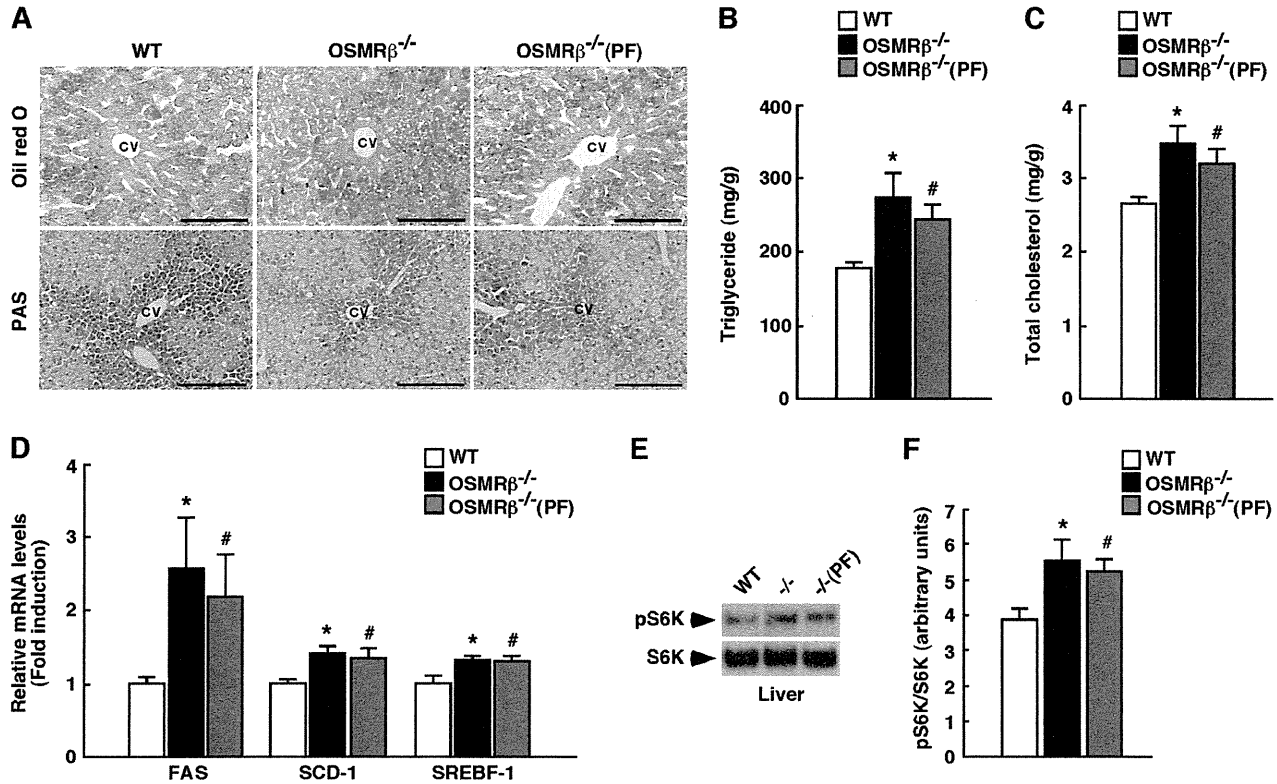

FIGURE 4. **Lipid metabolism in the livers of WT and OSMR$\beta^{-/-}$ mice under HFD conditions.** The mice (8 weeks old) were fed an HFD for 8 weeks. *A*, Oil Red O and PAS staining of the livers of WT, OSMR$\beta^{-/-}$, and OSMR$\beta^{-/-}$(PF) mice. *CV*, central vein. *Scale bar* = 100 μm. *B* and *C*, the content of triglycerides (*B*) and total cholesterol (*C*) in the livers of WT, OSMR$\beta^{-/-}$, and OSMR$\beta^{-/-}$(PF) mice in the fed state (n = 6). *D*, the expression levels of genes related to fatty acid synthesis (*FAS*, *SCD-1*, and *SREBF-1*) in the livers of WT, OSMR$\beta^{-/-}$, and OSMR$\beta^{-/-}$(PF) mice in the fed state (n = 6). *E*, Western blot analysis of phosphorylation of S6K (*pS6K*) in the livers of WT, OSMR$\beta^{-/-}$, and OSMR$\beta^{-/-}$(PF) mice in the fed state. *F*, a quantitative analysis of pS6K (n = 6). In the fed state, mice were fasted for 4 h before the experiments to eliminate the feeding effects on lipid metabolism. The data represent the mean ± S.E. *, $p < 0.05$ WT *versus* OSMR$\beta^{-/-}$ mice; #, $p < 0.05$ WT *versus* OSMR$\beta^{-/-}$(PF) mice, Student's *t* test.

tion of S6K in OSMR$\beta^{-/-}$ and OSMR$\beta^{-/-}$(PF) mice was maintained at the same levels as that observed in WT mice (Fig. 5*F*), suggesting that insulin signaling pathway related to lipogenesis was preserved in the liver of OSMR$\beta^{-/-}$ mice.

OSMR$\beta^{-/-}$ Mice Exhibit Hyperplasia of β-Cells in Pancreas under HFD Conditions—Histological examination of the pancreas revealed that the percentages of insulin-positive areas (β-cells) among total areas of the pancreas were higher in OSMR$\beta^{-/-}$ and OSMR$\beta^{-/-}$(PF) mice compared with those observed in WT mice (Fig. 5, *G* and *H*), suggesting that OSMR$\beta^{-/-}$ mice exhibit hyperplasia of β-cells in the pancreas. In addition, the expression of insulin mRNA was increased in the pancreas of OSMR$\beta^{-/-}$ and OSMR$\beta^{-/-}$(PF) mice compared with that in WT mice (Fig. 5*I*).

HFD Conditions Exacerbate Adipose Tissue Inflammation in OSMR$\beta^{-/-}$ Mice—The serum concentrations of TNF-α, IL-10, and serum amyloid A were higher in OSMR$\beta^{-/-}$ and OSMR$\beta^{-/-}$(PF) mice than those observed in WT mice at 8 weeks on the HFD (Table 1), indicating that the degree of systemic inflammation was elevated in OSMR$\beta^{-/-}$ and OSMR$\beta^{-/-}$(PF) mice. In the adipose tissue, the total number of F4/80-positive macrophages per weight of adipose tissue was higher in OSMR$\beta^{-/-}$ and OSMR$\beta^{-/-}$(PF) mice than those observed in WT mice (Fig. 6*A*). The percentages of both CD11c-positive M1-type macrophages and CD206-positive M2-type macrophages among the total number of F4/80-positive macrophages were higher in the adipose tissue of OSMR$\beta^{-/-}$ and OSMR$\beta^{-/-}$(PF) mice than in those of WT mice (Fig. 6, *B* and *C*). The percentages of CD11c/CD206-double-negative cells among the total number of F4/80-positive macrophages were lower in the adipose tissue of OSMR$\beta^{-/-}$ and OSMR$\beta^{-/-}$(PF) mice than in those of WT mice (Fig. 6*D*). In addition, the expression levels of inflammatory markers, including TNF-α, IL-1β, IFN-γ, MCP-1, CCR2, and TLR4, were higher in the adipose tissue and SVF of OSMR$\beta^{-/-}$ and OSMR$\beta^{-/-}$(PF) mice than those observed in WT mice, whereas there were no differences in the IL-6 expression levels between the three groups (Fig. 6, *E* and *F*). In contrast, the adiponectin expression level was lower in the adipose tissue and SVF of OSMR$\beta^{-/-}$ and OSMR$\beta^{-/-}$(PF) mice than in those of WT mice (Fig. 6, *E* and *F*). Unexpectedly, the expression levels of other anti-inflammatory markers, including IL-10, IL-13, MGL1, and MGL2, were also higher in the adipose tissue and SVF of OSMR$\beta^{-/-}$ and OSMR$\beta^{-/-}$(PF) mice than in those of WT mice (Fig. 6, *E* and *F*).

To determine whether the increases in anti-inflammatory markers were secondary to the preceding inflammatory response, we investigated the development of adipose tissue inflammation in OSMR$\beta^{-/-}$ mice at the earlier stage. At 4 weeks on the HFD (Fig. 7, *A* and *B*), the total number of

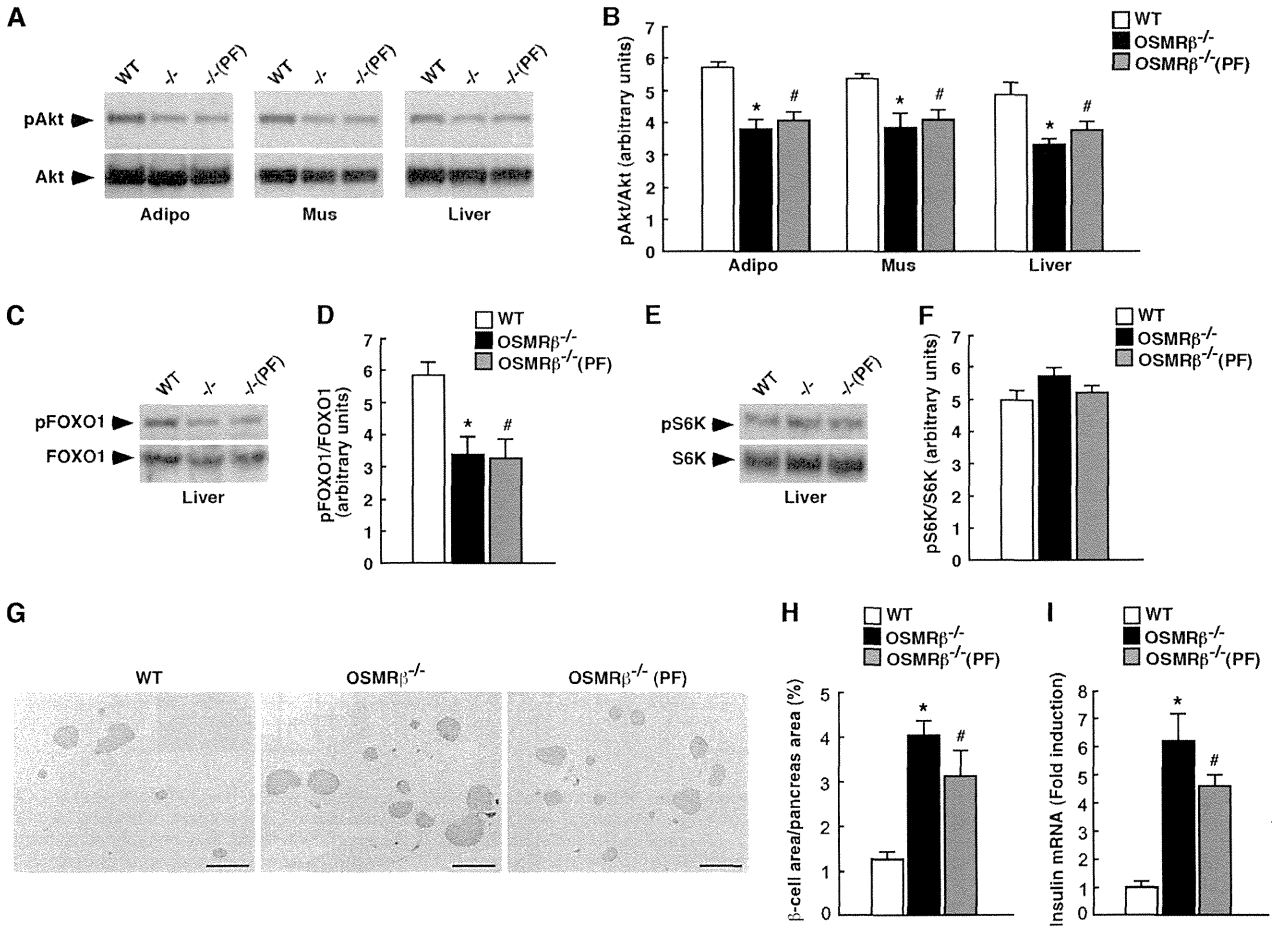

FIGURE 5. **Insulin signaling pathways in WT and OSMR$\beta^{-/-}$ mice at 8 weeks on the HFD.** After 24 h of fasting, mice were intraperitoneally injected with insulin (10 milliunits/g of body weight) and maintained for 10 min. *A*, insulin-stimulated Akt phosphorylation in the adipose tissues, skeletal muscles, and livers of WT, OSMR$\beta^{-/-}$, and OSMR$\beta^{-/-}$(PF) mice ($n = 6$). *B*, a quantitative analysis of pAkt ($n = 6$). *C–F*, insulin-stimulated phosphorylation of FOXO1 (*pFOXO1*) (C) and S6K (*pS6K*) (E) in the livers of WT, OSMR$\beta^{-/-}$, and OSMR$\beta^{-/-}$(PF) mice. A quantitative analysis of pFOXO1 (*D*) and pS6K (*F*) ($n = 6$) is shown. *G*, immunohistochemistry for insulin in the pancreas of WT, OSMR$\beta^{-/-}$, and OSMR$\beta^{-/-}$(PF) mice. *Scale bars* = 500 μm. *H*, quantitative analysis of the area of β-cells in the total area of the pancreas. *I*, the mRNA expression of insulin in the pancreas of WT, OSMR$\beta^{-/-}$, and OSMR$\beta^{-/-}$(PF) mice in the fed states. *Adipo*, adipose tissue; *Mus*, skeletal muscle. The data represent the mean ± S.E. *, $p < 0.05$ WT *versus* OSMRβ−/− mice; #, $p < 0.05$ WT *versus* OSMR$\beta^{-/-}$(PF) mice; Student's *t* test.

F4/80-positive macrophages per weight of adipose tissue and the percentage of CD11c-positive M1-type macrophages were increased in OSMR$\beta^{-/-}$ mice compared with those observed in WT mice. In addition, the expression levels of inflammatory markers, including TNF-α, IL-1β, IFN-γ, MCP-1, CCR2, and TLR4, were higher in the adipose tissue and SVF of OSMR$\beta^{-/-}$ mice than in those of WT mice at 4 weeks on the HFD (Fig. 7, *E* and *F*). In contrast, the percentage of CD206-positive M2-type macrophages was decreased in the adipose tissue of OSMR$\beta^{-/-}$ mice compared with that observed in WT mice at 4 weeks on the HFD (Fig. 7*C*). In addition, the expression levels of anti-inflammatory markers, including IL-10, IL-13, MGL1, and MGL2, were lower in the adipose tissue and SVF of OSMR$\beta^{-/-}$ mice than in those of WT mice at 4 weeks on the HFD (Fig. 7, *E* and *F*). There were no differences in the expression levels of IL-6 and adiponectin in the adipose tissue between WT and OSMR$\beta^{-/-}$ mice (Fig. 7, *E* and *F*). Such changes in the total number of ATMs, the polarization of ATMs, and cytokine production profiles were already observed in OSMR$\beta^{-/-}$ mice at 2 weeks on the HFD, when there was no difference in body weight between WT and OSMR$\beta^{-/-}$ mice (Fig. 7, *A–F*). There were no differences in the percentages of CD11c/CD206-double-negative cells among the total number of F4/80-positive macrophages in the adipose tissue between WT and OSMR$\beta^{-/-}$ mice at both 2 and 4 weeks on the HFD (Fig. 7*D*). Both glucose intolerance and insulin resistance were exacerbated in OSMR$\beta^{-/-}$ mice compared with those observed in WT mice at both 2 and 4 weeks on the HFD (Fig. 7, *G–N*). Therefore, the increases in the levels of anti-inflammatory markers observed at 8 weeks on the HFD were considered to reflect a secondary response to an earlier inflammatory reaction in the adipose tissue of OSMR$\beta^{-/-}$ mice.

Treatment with OSM Improves Insulin Resistance, Adipose Tissue Inflammation, and Hepatic Steatosis in Genetically Obese ob/ob Mice—To assess the effects of OSM on insulin resistance, adipose tissue inflammation, and hepatic steatosis in obese mice, OSM was intraperitoneally injected into *ob/ob* mice twice a day for 7 days. The body weights, adipose tissue weights, and liver weights were decreased in the OSM-treated

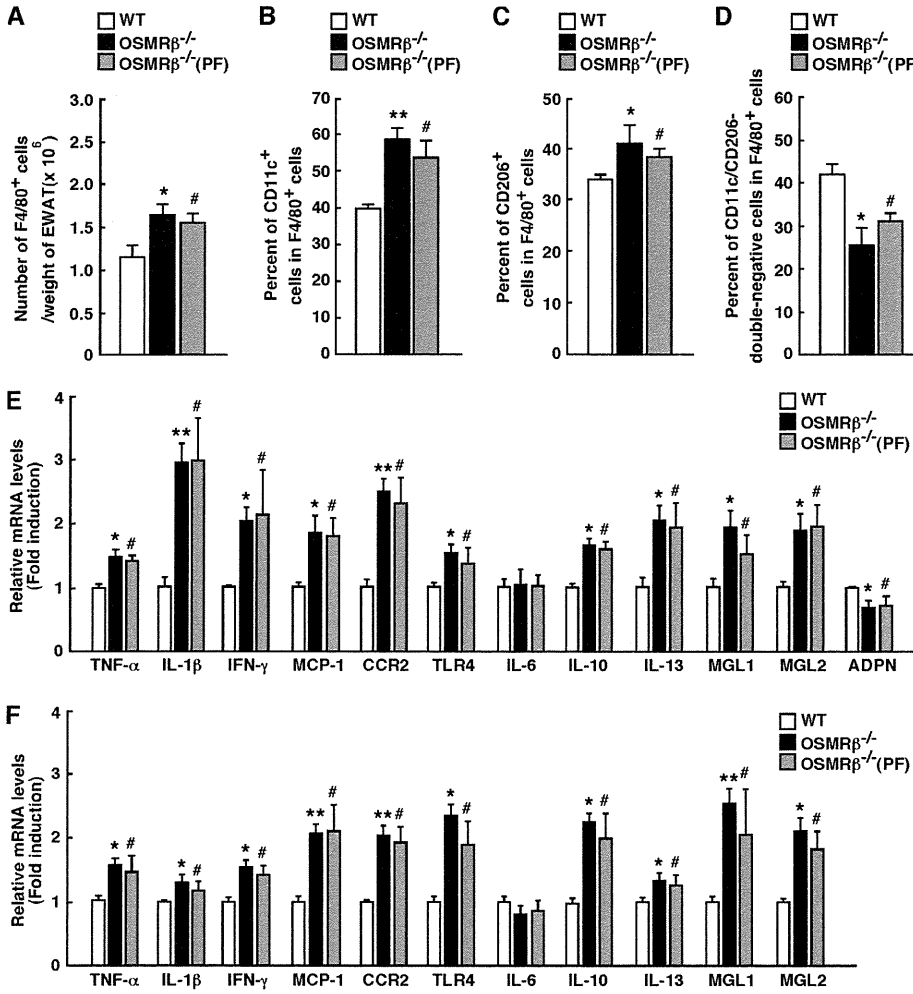

FIGURE 6. **Adipose tissue inflammation in WT and OSMRβ$^{-/-}$ mice at 8 weeks on the HFD.** The mice (8 weeks old) were fed an HFD for 8 weeks. *A*, total number of F4/80-positive cells per weights of adipose tissue in WT, OSMRβ$^{-/-}$, and OSMRβ$^{-/-}$(PF) mice ($n = 6$). *EWAT*, epididymal white adipose tissue. *B* and *C*, the percentages of CD11c-positive cells (*B*) and CD206-positive cells (*C*) among the F4/80-positive cells in WT, OSMRβ$^{-/-}$, and OSMRβ$^{-/-}$(PF) mice. *D*, the percentages of CD11c/CD206-double-negative cells among the F4/80-positive cells in WT, OSMRβ$^{-/-}$, and OSMRβ$^{-/-}$(PF) mice. *E* and *F*, the mRNA expression levels of inflammatory and anti-inflammatory markers (TNF-α, IL-1β, IFN-γ, CCR2, MCP-1, TLR4, IL-6, MGL1, MGL2, IL-10, IL-13, and adiponectin) in the adipose tissue (*E*) and SVF (*F*) of WT, OSMRβ$^{-/-}$, and OSMRβ$^{-/-}$(PF) mice ($n = 6$). *ADPN*, adiponectin. The data represent the mean ± S.E. *, $p < 0.05$; **, $p < 0.01$ WT *versus* OSMRβ−/− mice; #, $p < 0.05$ WT *versus* OSMRβ$^{-/-}$(PF) mice, Student's *t* test.

ob/*ob* mice compared with those observed in *ob*/*ob* mice with vehicle injection (Fig. 8, *A* and *B*). Both the blood glucose and serum insulin levels were also reduced by the treatment with OSM in the fasted state (Fig. 8, *C* and *D*). Treatment of *ob*/*ob* mice with OSM improved their glucose intolerance in an ipGTT (Fig. 8, *E* and *F*). The OSM-treated *ob*/*ob* mice were more sensitive to insulin, as measured by the ITT (Fig. 8, *G* and *H*). Therefore, OSM improves glucose intolerance and insulin resistance in *ob*/*ob* mice. In addition, the number of F4/80-positive macrophages per weight of adipose tissue was decreased in the adipose tissue by the treatment of OSM (Fig. 8*I*). The percentage of CD11c-positive M1-type macrophages was reduced, whereas the percentage of CD206-positive M2-type macrophages was increased in OSM-treated *ob*/*ob* mice (Fig. 8, *J* and *K*). In addition, OSM increased the expression of IL-10, IL-13, MGL1, and MGL2 in the adipose tissue of *ob*/*ob* mice (Fig. 8*L*). Furthermore, the Oil Red O staining revealed that lipid accumulation was reduced by the treatment of OSM in the liver of *ob*/*ob* mice (Fig. 8*M*). In contrast, the PAS staining showed that there were more glycogen granules in the hepatocytes of *ob*/*ob* mice treated with OSM compared with those observed in *ob*/*ob* mice with vehicle injection (Fig. 8*M*). In addition, the total cholesterol and triglyceride levels in the liver of *ob*/*ob* mice were decreased by the treatment of OSM (Fig. 8, *N* and *O*).

Direct Effects of OSM on the Liver of Genetically Obese ob/ob Mice—Consistent with the data in Fig. 1, *C* and *D*, the expression of OSMRβ was increased in the liver of the obese mice (Fig. 9, *A* and *B*). To investigate the direct effects of OSM on the liver of obese mice, we injected *ob*/*ob* mice with OSM intraportally. The activation of STAT3 was observed in the liver at 15 min after the intraportal injection of OSM (Fig. 9*C*). Furthermore, the expressions of both ACSL3 and ACSL5 were increased at 60 and 120 min after the intraportal injection of OSM (Fig. 9*D*). In addition, OSM decreased the expression of FAS in the liver of *ob*/*ob* mice (Fig. 9*D*). These results suggest that OSM directly acts on the liver in obese mice.

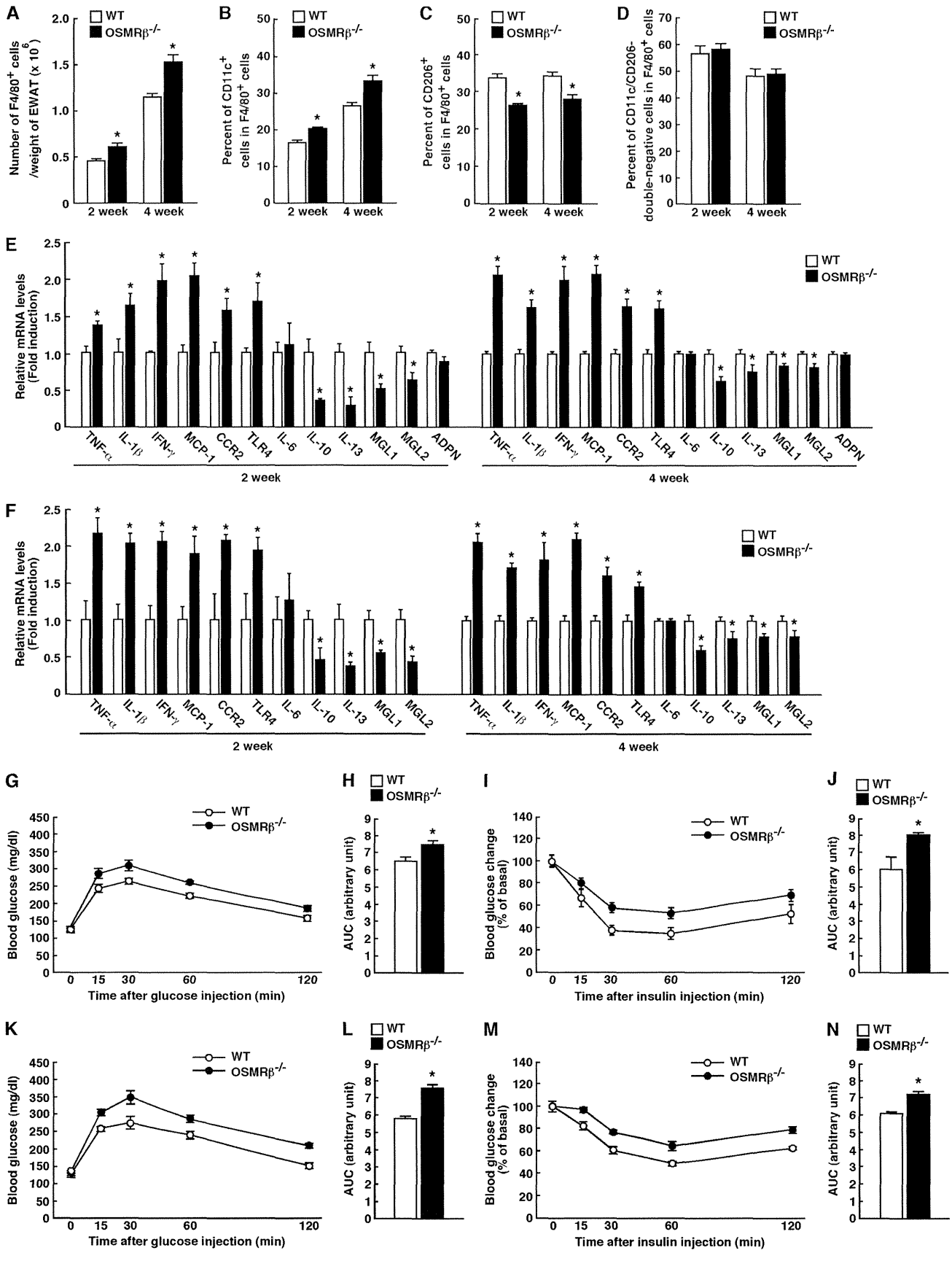
A
Number of F4/80+ cells /weight of EWAT (x 10^6)
WT
OSMRβ-/-
2 week
4 week
B
Percent of CD11c+ cells in F4/80+ cells
C
Percent of CD206+ cells in F4/80+ cells
D
Percent of CD11c/CD206-double-negative cells in F4/80+ cells
E
Relative mRNA levels (Fold induction)
TNF-α
IL-1β
IFN-γ
MCP-1
CCR2
TLR4
IL-6
IL-10
IL-13
MGL1
MGL2
ADPN
F
G
Blood glucose (mg/dl)
Time after glucose injection (min)
H
AUC (arbitrary unit)
I
Blood glucose change (% of basal)
Time after insulin injection (min)
J
K
L
M
N

DISCUSSION

OSM is a member of the IL-6 family of cytokines and plays a role in a variety of physiological functions, including hematopoiesis, the development of neurons, and the modulation of inflammatory responses (20, 30–32). Some members of this family, such as IL-6, ciliary neurotrophic factor, and cardiotrophin-1, are known to be associated with the development of obesity and insulin resistance (33–35). Although we have demonstrated the expression of OSMRβ in ATMs and its association with systemic insulin resistance in a previous report (21), the role of OSM signaling in the development of obesity and related metabolic disorders remains unclear. In the present study we first examined the expression of OSMRβ in the various tissues of both DIO and genetically obese *ob/ob* mice. The expression of OSMRβ was increased in the adipose tissue and liver of in these obese mice compared with their control mice. In the adipose tissue, OSMRβ was increased in the SVF, especially in the F4/80-positive ATMs, in both models of obese mice. These results suggest that OSM signaling is strongly associated with the pathogenesis of obesity and related metabolic disorders.

Next, we analyzed metabolic parameters in OSMRβ$^{-/-}$ mice fed the HFD. Strikingly, feeding an HFD for 8 weeks resulted in more severe obesity in OSMRβ$^{-/-}$ mice than in WT mice. Hyperglycemia, hyperinsulinemia, insulin resistance, adipose tissue inflammation, and hepatic steatosis were exacerbated in OSMRβ$^{-/-}$ mice under HFD conditions. In addition, OSM improved adipose tissue inflammation, insulin resistance, and hepatic steatosis of *ob/ob* mice. These results suggest that OSM signaling has suppressive effects on the deterioration of obesity and related metabolic disorders.

Obesity is an important cause of the development of metabolic disorders (2). In the past decade, it has been widely accepted that HFD leads to obesity that causes chronic low-grade inflammation followed by insulin resistance (2). Then, insulin resistance leads to hyperinsulinemia and β cell failure successively, resulting in various metabolic disorders, including type 2 diabetes and hepatic steatosis. Therefore, there is the possibility that the deterioration of metabolic disorders noted in OSMRβ$^{-/-}$ mice was due to the increase in fat mass. However, the pair-feeding study revealed that none of the metabolic disorders observed in OSMRβ$^{-/-}$ mice fed the HFD, including adipose tissue inflammation, insulin resistance, and hepatic steatosis, was affected by the decrease in food intake and body weight in OSMRβ$^{-/-}$ mice pair-fed with WT mice. These results suggest that the effects of OSM signaling on the deterioration of metabolic disorders associated with diet-induced obesity are independent of changes in food intake and body weight. In addition, the deterioration of adipose tissue inflammation, hyperinsulinemia, insulin resistance, and glucose intolerance were already observed in OSMRβ$^{-/-}$ mice at 2 weeks on the HFD, when there was no difference in body weight between WT and OSMRβ$^{-/-}$ mice. Recently, Mehran *et al.* (36) have proposed a novel model of obesity and type 2 diabetes distinct from the widely accepted model in which hyperinsulinemia is upstream of obesity. Thus, the relationships between obesity, insulin resistance, and hyperinsulinemia need to be revisited, and we are considering OSMRβ$^{-/-}$ mice as a unique mouse model of metabolic diseases.

Under conditions of obesity, inflammatory cytokines, such as TNF-α, IL-1β, and IFN-γ, are primarily secreted from M1-type ATMs, which induces insulin resistance (7–11, 37, 38). In contrast, an anti-inflammatory cytokine, IL-10, is produced by M2-type ATMs, which suppresses insulin resistance (7, 12, 13). In our previous study OSM signaling was found to have a suppressive effect on adipose tissue inflammation due to the polarization of the macrophage phenotype to the M2-type under normal dietary conditions (21). In the present study feeding an HFD induced the expression of OSMRβ in ATMs, suggesting the important role of OSM in the development of adipose tissue inflammation under conditions of obesity. As expected, OSMRβ$^{-/-}$ mice, in which OSM signaling is deleted, exhibited increases in both the number of M1-type ATMs and expression levels of inflammatory cytokines in the adipose tissue when fed the HFD for 8 weeks. At this stage, insulin resistance was exacerbated in OSMRβ$^{-/-}$ mice compared with that observed in WT mice, suggesting that adipose tissue inflammation enhanced by M1-type ATMs may contribute to the exacerbation of insulin resistance in OSMRβ$^{-/-}$ mice. Recently, it has been reported that these inflammatory and anti-inflammatory cytokines are produced by other types of cells, such as regulatory T cells and CD8-positive T cells, and play important roles in the development of obesity-related metabolic disorders (5, 39). We cannot exclude the possibility that the changes in cytokine production profiles result from the other cells except for ATMs in OSMRβ$^{-/-}$ mice. However, it is possible that ATMs are responsible for the inflammatory cytokine production profiles in OSMRβ$^{-/-}$ mice directly because OSMRβ was exclusively expressed in F4/80-positive macrophages on adipose tissues under obese conditions.

On the other hand, the number of M2-type macrophages and the expression level of IL-10 were also increased in the adipose tissue of OSMRβ$^{-/-}$ mice compared with those observed in WT mice. As the inflammatory responses driven by M1-type macrophages are often counteracted by protective mechanisms operated by M2-type macrophages (40), we analyzed the degree of adipose tissue inflammation and insulin resistance in OSMRβ$^{-/-}$ mice at an early stage of HFD. At 4 weeks on the HFD, the number of M2-type macrophages and the expression levels of anti-inflammatory cytokines were low in the adipose tissue of OSMRβ$^{-/-}$ mice compared with that observed in WT mice, whereas OSMRβ$^{-/-}$ mice exhibited an increased num-

FIGURE 7. **Adipose tissue inflammation and glucose metabolism in WT and OSMRβ$^{-/-}$ mice at 2 and 4 weeks on the HFD.** *A*, total number of F4/80-positive cells per weights of adipose tissue in WT and OSMRβ$^{-/-}$ mice ($n = 6$). *B* and *C*, the percentages of CD11c-positive cells (*B*) and CD206-positive cells (*C*) among the F4/80-positive cells in WT and OSMRβ$^{-/-}$ mice. *D*, the percentages of CD11c/CD206-double-negative cells among the F4/80-positive cells in WT and OSMRβ$^{-/-}$ mice. *E* and *F*, the mRNA expression levels of inflammatory and anti-inflammatory markers (TNF-α, IL-1β, IFN-γ, CCR2, MCP-1, TLR4, IL-6, MGL1, MGL2, IL-10, IL-13, and adiponectin) in the adipose tissue (*E*) and SVF (*F*) of WT and OSMRβ$^{-/-}$ mice ($n = 6$). *G–N*, the results of the ipGTTs (*G* and *K*) and ITTs (*I* and *M*) in WT and OSMRβ$^{-/-}$ mice at 2 weeks (*G–J*) and 4 weeks (*K–N*) on the HFD ($n = 6$). The AUC for blood glucose on the ipGTTs (*H* and *L*) and ITTs (*J* and *N*) was shown. *ADPN*, adiponectin. The data represent the mean ± S.E. *, $p < 0.05$; **, $p < 0.01$ WT *versus* OSMRβ$^{-/-}$ mice, Student's *t* test.

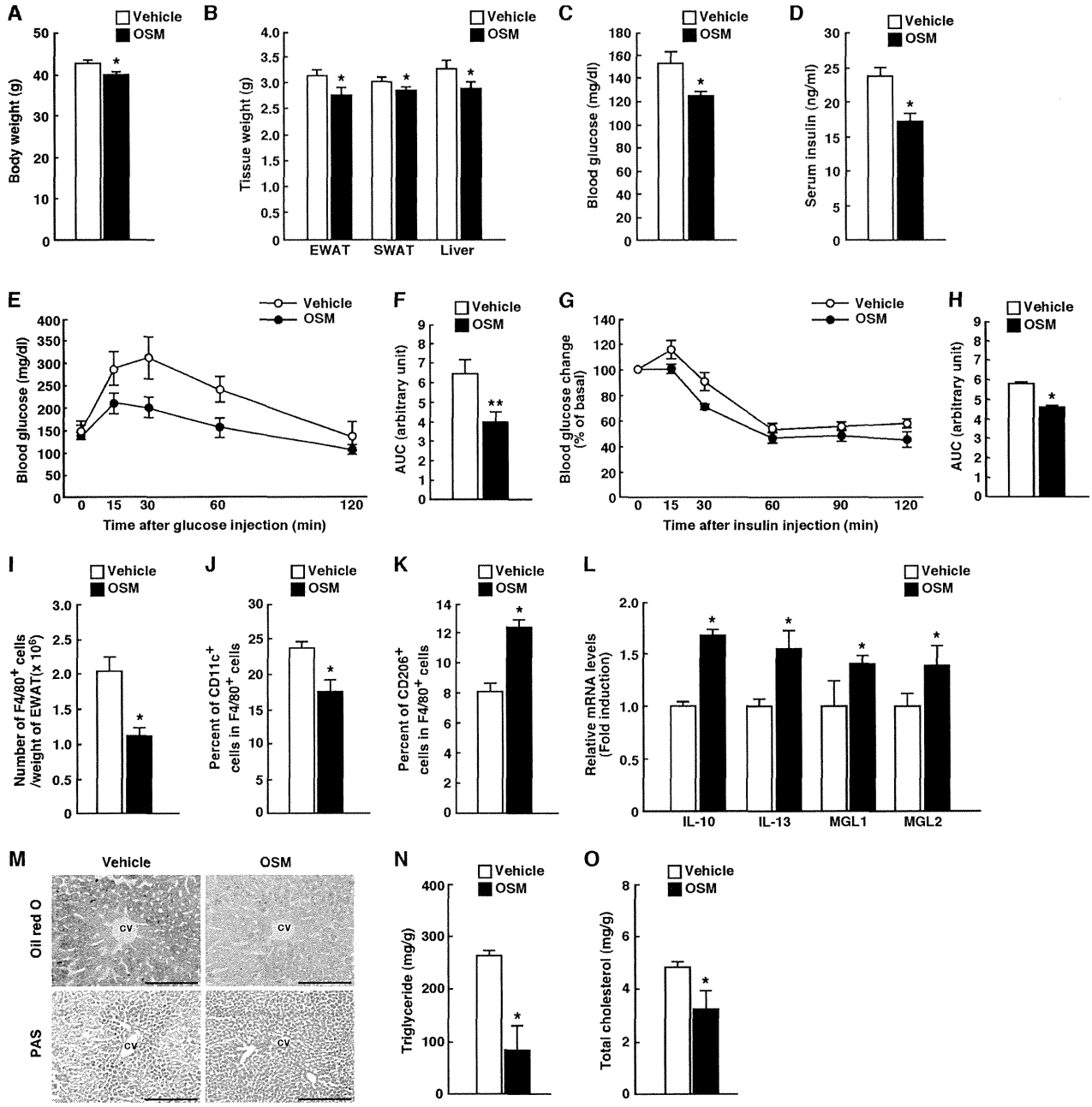

FIGURE 8. **The effects of OSM on glucose metabolism, adipose tissue inflammation, and hepatic steatosis in *ob/ob* mice.** *ob/ob* mice were injected intraperitoneally with either vehicle or recombinant mouse OSM (12.5 ng/g of body weight) twice a day for 7 days. *A*, the body weights in vehicle- and OSM-treated *ob/ob* mice ($n = 6$). *B*, the tissue weights in vehicle- and OSM-treated *ob/ob* mice ($n = 6$). *EWAT*, epididymal white adipose tissue; *SWAT*, subcutaneous white adipose tissue. *C* and *D*, blood glucose (*C*) and serum insulin (*D*) levels in vehicle- and OSM-treated *ob/ob* mice in the fasted states ($n = 6$). In the fasted states, mice were fasted overnight before the experiments. *E–H*, the results of the ipGTTs (*E*) and ITTs (*G*) in vehicle- and OSM-treated *ob/ob* mice ($n = 6$). The AUC for blood glucose on the ipGTTs (*F*) and ITTs (*H*) is shown. For ipGTTs, mice were fasted for 16 h and intraperitoneally injected with D-glucose (0.5 g/kg of body weight). For ITTs, mice were fasted for 4 h and intraperitoneally injected with insulin (5 unit/kg of body weight). *I*, total number of F4/80-positive cells per weights of adipose tissue in vehicle- and OSM-treated *ob/ob* mice ($n = 6$). *J* and *K*, the percentages of CD11c-positive cells (*J*) and CD206-positive cells (*K*) among the F4/80-positive cells in vehicle- and OSM-treated *ob/ob* mice. *L*, the mRNA expression levels of anti-inflammatory markers (IL-10, IL-13, MGL1, and MGL2) in the adipose tissue of vehicle- and OSM-treated *ob/ob* mice ($n = 6$). *M*, Oil Red O and PAS staining of the livers of vehicle- and OSM-treated *ob/ob* mice. *CV*, central vein. *Scale bar* = 100 μm. *N* and *O*, the content of triglycerides (*N*) and total cholesterol (*O*) in the livers of vehicle- and OSM-treated *ob/ob* mice in the fed state ($n = 6$). In the fed state, mice were fasted for 4 h before the experiments to eliminate the feeding effects on lipid metabolism. The data represent the mean ± S.E. *, $p < 0.05$; **, $p < 0.01$ vehicle *versus* OSM, Student's *t* test.

ber of M1-type ATMs, high expression levels of inflammatory cytokines, and severe insulin resistance. Therefore, the increased anti-inflammatory responses observed in OSMR$\beta^{-/-}$ mice at 8 weeks on the HFD may have occurred to counteract the excessive inflammation induced by the larger number of M1-type ATMs and the up-regulation of inflammatory cytokines in the adipose tissue. In addition, an increased total number of ATMs, the polarization of ATMs to M1-type,

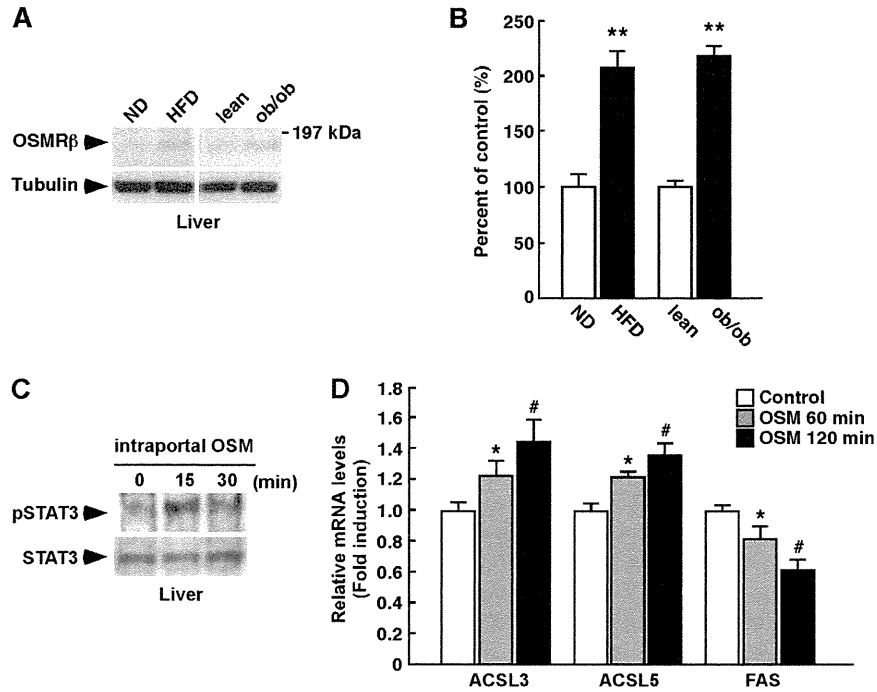

FIGURE 9. **The direct effects of OSM on liver lipid metabolism in *ob/ob* mice.** *ob/ob* mice were injected intraportally with either vehicle or recombinant mouse OSM (12.5 ng/g of body weight) and maintained for 60 and 120 min. *A*, Western blot analysis of OSMRβ in the liver in the WT mice fed a normal diet (*ND*) or an HFD and the lean and *ob/ob* mice ($n = 6$). The apparent molecular masses are indicated on the *right*. *B*, a quantitative analysis of the protein expression of OSMRβ in the liver ($n = 6$). *C*, activation of STAT3 in the liver by the intraportal injection of OSM in *ob/ob* mice. *D*, the mRNA expression levels of genes related to lipolysis (*ACSL3* and *ACSL5*) and lipogenesis (*FAS*) in the liver of vehicle- and OSM-injected *ob/ob* mice ($n = 6$). The data represent the mean ± S.E. **, $p < 0.01$ normal diet (*ND*) *versus* HFD or lean *versus ob/ob* (*B*); *, $p < 0.05$ vehicle *versus* OSM 60 min; #, $p < 0.05$ vehicle *versus* OSM 120 min; Student's *t* test.

and inflammatory cytokine production profiles were already observed in OSMR$\beta^{-/-}$ mice at 2 weeks on the HFD. At this stage, hyperinsulinemia, glucose intolerance, and insulin resistance in OSMR$\beta^{-/-}$ mice were more severe than those in WT mice despite no differences in body weight between two genotypes, suggesting that the deterioration of these metabolic disturbances in OSMR$\beta^{-/-}$ mice occurs independent of the increase in body weight.

Obesity-induced insulin resistance causes serious metabolic disorders, including cardiovascular disease and hepatic steatosis (1, 41). Hepatic steatosis, in particular, is a predisposing factor for non-alcoholic steatohepatitis, which often progresses to liver cirrhosis and hepatocellular carcinoma (42). In the present study, OSMR$\beta^{-/-}$ mice fed an HFD for 8 weeks exhibited severe hepatic steatosis compared with that observed in WT mice. The expression levels of the transcription factor, SREBF-1, and its target genes, FAS and SCD-1, were also increased in the liver of OSMR$\beta^{-/-}$ mice. As FAS and SCD-1 promote fatty acid synthesis in the liver, increased *de novo* lipogenesis in the liver may result in the deterioration of hepatic steatosis in OSMR$\beta^{-/-}$ mice. Furthermore, insulin stimulates *de novo* lipogenesis by increasing the expression of SREBF-1 (43). We observed that the serum concentration of insulin was high in OSMR$\beta^{-/-}$ mice compared with those observed in WT mice, suggesting that the up-regulation of insulin induces an increased expression of SREBF-1 in OSMR$\beta^{-/-}$ mice. Therefore, hepatic steatosis is likely exacerbated in HFD-fed OSMR$\beta^{-/-}$ mice due to the promotion of hepatic lipogenesis.

It has been long accepted that insulin resistance and hepatic steatosis are mutually related in a "vicious cycle" (41). On the other hand, some investigators have recently reported the dissociation of hepatic steatosis from insulin resistance (44); insulin resistance without hepatic steatosis (with hypotriglycemia) has been observed in liver-specific insulin receptor knock-out mice (45, 46) and the liver-specific deletion of phosphatase and tensin homolog has been found to improve systemic insulin resistance associated with enhanced hepatic steatosis (47). Hence, hepatic steatosis is not always related to insulin resistance. To address this issue, Brown and Goldstein (48) proposed the concept of "selective insulin resistance." When insulin signaling is completely blunted in the liver, hepatic gluconeogenesis is promoted, and hepatic lipogenesis is inhibited. However, when some steps of insulin signaling only required for the suppression of hepatic gluconeogenesis are blunted in liver, the remaining intact mechanisms of insulin signaling drive hepatic lipogenesis. In the present study, we demonstrated that the activation of FOXO1 due to stimulation with insulin, which suppresses the gluconeogenetic actions of insulin, was inhibited in the liver of OSMR$\beta^{-/-}$ mice compared with that observed in WT mice. On the other hand, the phosphorylation of S6K after stimulation with insulin, which promotes *de novo* lipogenesis, remained intact in the liver of OSMR$\beta^{-/-}$ mice. As the degree of hyperinsulinemia was much more severe in OSMR$\beta^{-/-}$ mice than in WT mice, selective insulin resistance may contribute to the progression of hepatic steatosis in OSMR$\beta^{-/-}$ mice. Of course, we cannot rule out the possibility that other pathways may induce *de novo* lipogenesis in the liver, including glucose-induced carbohydrate response element-binding protein activation (49) and/or cholesterol-induced liver X receptor activation (50).

Alternatively, the cause of severe hepatic steatosis in OSMR$\beta^{-/-}$ mice is the lack of direct effects of OSM on the liver. In the present study, we observed that OSMRβ was up-regulated in the liver of obese mice. To test the direct effects of OSM on the liver, we injected OSM intraportally in *ob/ob* mice. A signal molecule for the downstream of OSMRβ, STAT3, was activated in the liver by the intraportal injection of OSM. Zhou *et al.* (51) have reported that the expression of ACSL3 and ACSL5, which promote lipolysis in the liver, is increased by OSM in HepG2 cells. In the present study, the intraportal injection of OSM increased the expression of ACSL3 and ACSL5 in the liver of obese mice. In addition, OSM decreased the expression of FAS in the liver. Thus, OSM may directly increase lipolysis and suppresses lipogenesis in the liver of obese mice.

In conclusion, OSMR$\beta^{-/-}$ mice exhibited severe obesity, adipose tissue inflammation, insulin resistance, and hepatic steatosis under HFD conditions. In addition, OSM improved adipose tissue inflammation, insulin resistance, and hepatic steatosis in genetically obese *ob/ob* mice. Our results strongly suggest that OSMRβ is required to protect against the development of obesity and related metabolic disorders. Therefore, OSM signaling is a potential novel therapeutic target in patients with metabolic syndrome, including obesity, insulin resistance, and hepatic steatosis.

REFERENCES

1. Bornfeldt, K. E., and Tabas, I. (2011) Insulin resistance, hyperglycemia, and atherosclerosis. *Cell Metab.* **14,** 575–585
2. Osborn, O., and Olefsky, J. M. (2012) The cellular and signaling networks linking the immune system and metabolism in disease. *Nat. Med.* **18,** 363–374
3. Weisberg, S. P., McCann, D., Desai, M., Rosenbaum, M., Leibel, R. L., and Ferrante, A. W., Jr. (2003) Obesity is associated with macrophage accumulation in adipose tissue. *J. Clin. Invest.* **112,** 1796–1808
4. Talukdar, S., Oh da, Y., Bandyopadhyay, G., Li, D., Xu, J., McNelis, J., Lu, M., Li, P., Yan, Q., Zhu, Y., Ofrecio, J., Lin, M., Brenner, M. B., and Olefsky, J. M. (2012) Neutrophils mediate insulin resistance in mice fed a high-fat diet through secreted elastase. *Nat. Med.* **18,** 1407–1412
5. Nishimura, S., Manabe, I., Nagasaki, M., Eto, K., Yamashita, H., Ohsugi, M., Otsu, M., Hara, K., Ueki, K., Sugiura, S., Yoshimura, K., Kadowaki, T., and Nagai, R. (2009) CD8+ effector T cells contribute to macrophage recruitment and adipose tissue inflammation in obesity. *Nat. Med.* **15,** 914–920
6. Wu, D., Molofsky, A. B., Liang, H. E., Ricardo-Gonzalez, R. R., Jouihan, H. A., Bando, J. K., Chawla, A., and Locksley, R. M. (2011) Eosinophils sustain adipose alternatively activated macrophages associated with glucose homeostasis. *Science* **332,** 243–247
7. Fujisaka, S., Usui, I., Bukhari, A., Ikutani, M., Oya, T., Kanatani, Y., Tsuneyama, K., Nagai, Y., Takatsu, K., Urakaze, M., Kobayashi, M., and Tobe, K. (2009) Regulatory mechanisms for adipose tissue M1 and M2 macrophages in diet-induced obese mice. *Diabetes* **58,** 2574–2582
8. de Alvaro, C., Teruel, T., Hernandez, R., and Lorenzo, M. (2004) Tumor necrosis factor α produces insulin resistance in skeletal muscle by activation of inhibitor κB kinase in a p38 MAPK-dependent manner. *J. Biol. Chem.* **279,** 17070–17078
9. Nguyen, M. T., Satoh, H., Favelyukis, S., Babendure, J. L., Imamura, T., Sbodio, J. I., Zalevsky, J., Dahiyat, B. I., Chi, N. W., and Olefsky, J. M. (2005) JNK and tumor necrosis factor-α mediate free fatty acid-induced insulin resistance in 3T3-L1 adipocytes. *J. Biol. Chem.* **280,** 35361–35371
10. Stienstra, R., Joosten, L. A., Koenen, T., van Tits, B., van Diepen, J. A., van den Berg, S. A., Rensen, P. C., Voshol, P. J., Fantuzzi, G., Hijmans, A., Kersten, S., Müller, M., van den Berg, W. B., van Rooijen, N., Wabitsch, M., Kullberg, B. J., van der Meer, J. W., Kanneganti, T., Tack, C. J., and Netea, M. G. (2010) The inflammasome-mediated caspase-1 activation controls adipocyte differentiation and insulin sensitivity. *Cell Metab.* **12,** 593–605
11. Jager, J., Grémeaux, T., Cormont, M., Le Marchand-Brustel, Y., and Tanti, J. F. (2007) Interleukin-1β-induced insulin resistance in adipocytes through down-regulation of insulin receptor substrate-1 expression. *Endocrinology* **148,** 241–251
12. Hong, E. G., Ko, H. J., Cho, Y. R., Kim, H. J., Ma, Z., Yu, T. Y., Friedline, R. H., Kurt-Jones, E., Finberg, R., Fischer, M. A., Granger, E. L., Norbury, C. C., Hauschka, S. D., Philbrick, W. M., Lee, C. G., Elias, J. A., and Kim, J. K. (2009) Interleukin-10 prevents diet-induced insulin resistance by attenuating macrophage and cytokine response in skeletal muscle. *Diabetes* **58,** 2525–2535
13. Gao, M., Zhang, C., Ma, Y., Bu, L., Yan, L., and Liu, D. (2013) Hydrodynamic delivery of mIL10 gene protects mice from high-fat diet-induced obesity and glucose intolerance. *Mol. Ther.* **21,** 1852–1861
14. Taga, T., and Kishimoto, T. (1997) Gp130 and the interleukin-6 family of cytokines. *Annu. Rev. Immunol.* **15,** 797–819
15. Tanaka, M., Hara, T., Copeland, N. G., Gilbert, D. J., Jenkins, N. A., and Miyajima, A. (1999) Reconstitution of the functional mouse oncostatin M (OSM) receptor: molecular cloning of the mouse OSM receptor β subunit. *Blood* **93,** 804–815
16. Tamura, S., Morikawa, Y., Miyajima, A., and Senba, E. (2002) Expression of oncostatin M in hematopoietic organs. *Dev. Dyn.* **225,** 327–331
17. Repovic, P., and Benveniste, E. N. (2002) Prostaglandin E2 is a novel inducer of oncostatin-M expression in macrophages and microglia. *J. Neurosci.* **22,** 5334–5343
18. Broxmeyer, H. E., Bruns, H. A., Zhang, S., Cooper, S., Hangoc, G., McKenzie, A. N., Dent, A. L., Schindler, U., Naeger, L. K., Hoey, T., and Kaplan, M. H. (2002) Th1 cells regulate hematopoietic progenitor cell homeostasis by production of oncostatin M. *Immunity* **16,** 815–825
19. Mozaffarian, A., Brewer, A. W., Trueblood, E. S., Luzina, I. G., Todd, N. W., Atamas, S. P., and Arnett, H. A. (2008) Mechanisms of oncostatin M-induced pulmonary inflammation and fibrosis. *J. Immunol.* **181,** 7243–7253
20. Wallace, P. M., MacMaster, J. F., Rouleau, K. A., Brown, T. J., Loy, J. K., Donaldson, K. L., and Wahl, A. F. (1999) Regulation of inflammatory responses by oncostatin M. *J. Immunol.* **162,** 5547–5555
21. Komori, T., Tanaka, M., Senba, E., Miyajima, A., and Morikawa, Y. (2013) Lack of oncostatin M receptor β leads to adipose tissue inflammation and insulin resistance by switching macrophage phenotype. *J. Biol. Chem.* **288,** 21861–21875
22. Tanaka, M., Hirabayashi, Y., Sekiguchi, T., Inoue, T., Katsuki, M., and Miyajima, A. (2003) Targeted disruption of oncostatin M receptor results in altered hematopoiesis. *Blood* **102,** 3154–3162
23. Racioppi, L., Noeldner, P. K., Lin, F., Arvai, S., Means, A. R. (2012) Calcium/calmodulin-dependent protein kinase kinase 2 regulates macrophage-mediated inflammatory responses. *J. Biol. Chem.* **287,** 11579–11591
24. Komori, T., Doi, A., Nosaka, T., Furuta, H., Akamizu, T., Kitamura, T., Senba, E., and Morikawa, Y. (2012) Regulation of AMP-activated protein kinase signaling by AFF4 protein, member of AF4 (ALL1-fused gene from chromosome 4) family of transcription factors, in hypothalamic neurons. *J. Biol. Chem.* **287,** 19985–19996
25. Komori, T., Doi, A., Furuta, H., Wakao, H., Nakao, N., Nakazato, M., Nanjo, K., Senba, E., and Morikawa, Y. (2010) Regulation of ghrelin signaling by a leptin-induced gene, negative regulatory element-binding protein, in the hypothalamic neurons. *J. Biol. Chem.* **285,** 37884–37894
26. Folch, J., Lees, M., and Sloane Stanley, G. H. (1957) A simple method for the isolation and purification of total lipides from animal tissues. *J. Biol. Chem.* **226,** 497–509
27. Owen, J. L., Zhang, Y., Bae, S. H., Farooqi, M. S., Liang, G., Hammer, R. E., Goldstein, J. L., and Brown, M. S. (2012) Insulin stimulation of SREBP-1c processing in transgenic rat hepatocytes requires p70 S6-kinase. *Proc. Natl. Acad. Sci. U.S.A.* **109,** 16184–16189
28. Puigserver, P., Rhee, J., Donovan, J., Walkey, C. J., Yoon, J. C., Oriente, F., Kitamura, Y., Altomonte, J., Dong, H., Accili, D., Spiegelman, B. M. (2003) Insulin-regulated hepatic gluconeogenesis through FOXO1-PGC-1α interaction. *Nature* **423,** 550–555
29. Bae, E. J., Xu, J., Oh, D. Y., Bandyopadhyay, G., Lagakos, W. S., Keshwani,

M., Olefsky, J. M. (2012) Liver-specific p70 S6 kinase depletion protects against hepatic steatosis and systemic insulin resistance. *J. Biol. Chem.* **287,** 18769–18780
30. Kamiya, A., Kinoshita, T., Ito, Y., Matsui, T., Morikawa, Y., Senba, E., Nakashima, K., Taga, T., Yoshida, K., Kishimoto, T., and Miyajima, A. (1999) Fetal liver development requires a paracrine action of oncostatin M through the gp130 signal transducer. *EMBO J.* **18,** 2127–2136
31. Morikawa, Y., Tamura, S., Minehata, K., Donovan, P. J., Miyajima, A., and Senba, E. (2004) Essential function of oncostatin m in nociceptive neurons of dorsal root ganglia. *J. Neurosci.* **24,** 1941–1947
32. Mukouyama, Y., Hara, T., Xu, M., Tamura, K., Donovan, P. J., Kim, H., Kogo, H., Tsuji, K., Nakahata, T., and Miyajima, A. (1998) *In vitro* expansion of murine multipotential hematopoietic progenitors from the embryonic aorta-gonad-mesonephros region. *Immunity* **8,** 105–114
33. Wallenius, V., Wallenius, K., Ahrén, B., Rudling, M., Carlsten, H., Dickson, S. L., Ohlsson, C., and Jansson, J. O. (2002) Interleukin-6-deficient mice develop mature-onset obesity. *Nat. Med.* **8,** 75–79
34. Watt, M. J., Dzamko, N., Thomas, W. G., Rose-John, S., Ernst, M., Carling, D., Kemp, B. E., Febbraio, M. A., and Steinberg, G. R. (2006) CNTF reverses obesity-induced insulin resistance by activating skeletal muscle AMPK. *Nat. Med.* **12,** 541–548
35. Moreno-Aliaga, M. J., Pérez-Echarri, N., Marcos-Gómez, B., Larequi, E., Gil-Bea, F. J., Viollet, B., Gimenez, I., Martínez, J. A., Prieto, J., and Bustos, M. (2011) Cardiotrophin-1 is a key regulator of glucose and lipid metabolism. *Cell Metab.* **14,** 242–253
36. Mehran, A. E., Templeman, N. M., Brigidi, G. S., Lim, G. E., Chu, K. Y., Hu, X., Botezelli, J. D., Asadi, A., Hoffman, B. G., Kieffer, T. J., Bamji, S. X., Clee, S. M., Johnson, J. D. (2012) Hyperinsulinemia drives diet-induced obesity independently of brain insulin production. *Cell Metab.* **16,** 723–737
37. O'Rourke, R. W., White, A. E., Metcalf, M. D., Winters, B. R., Diggs, B. S., Zhu, X., and Marks, D. L. (2012) Systemic inflammation and insulin sensitivity in obese IFN-γ knockout mice. *Metabolism* **61,** 1152–1161
38. Grzelkowska-Kowalczyk, K., and Wieteska-Skrzeczyńska, W. (2010) Treatment with IFN-γ prevents insulin-dependent PKB, p70S6k phosphorylation and protein synthesis in mouse C2C12 myogenic cells. *Cell Biol. Int.* **34,** 117–124
39. Feuerer, M., Herrero, L., Cipolletta, D., Naaz, A., Wong, J., Nayer, A., Lee, J., Goldfine, A. B., Benoist, C., Shoelson, S., Mathis, D. (2009) Lean, but not obese, fat is enriched for a unique population of regulatory T cells that affect metabolic parameters. *Nat. Med.* **15,** 930–939
40. Goerdt, S., and Orfanos, C. E. (1999) Other functions, other genes: alternative activation of antigen-presenting cells. *Immunity* **10,** 137–142
41. Tilg, H., and Moschen, A. R. (2008) Insulin resistance, inflammation, and non-alcoholic fatty liver disease. *Trends Endocrinol. Metab.* **19,** 371–379
42. Michelotti, G. A., Machado, M. V., and Diehl, A. M. (2013) NAFLD, NASH, and liver cancer. *Nat. Rev. Gastroenterol. Hepatol.* **10,** 656–665
43. Li, S., Brown, M. S., and Goldstein, J. L. (2010) Bifurcation of insulin signaling pathway in rat liver: mTORC1 required for stimulation of lipogenesis, but not inhibition of gluconeogenesis. *Proc. Natl. Acad. Sci. U.S.A.* **107,** 3441–3446
44. Sun, Z., and Lazar, M. A. (2013) Dissociating fatty liver and diabetes. *Trends Endocrinol. Metab.* **24,** 4–12
45. Michael, M. D., Kulkarni, R. N., Postic, C., Previs, S. F., Shulman, G. I., Magnuson, M. A., and Kahn, C. R. (2000) Loss of insulin signaling in hepatocytes leads to severe insulin resistance and progressive hepatic dysfunction. *Mol. Cell* **6,** 87–97
46. Biddinger, S. B., Hernandez-Ono, A., Rask-Madsen, C., Haas, J. T., Alemán, J. O., Suzuki, R., Scapa, E. F., Agarwal, C., Carey, M. C., Stephanopoulos, G., Cohen, D. E., King, G. L., Ginsberg, H. N., and Kahn, C. R. (2008) Hepatic insulin resistance is sufficient to produce dyslipidemia and susceptibility to atherosclerosis. *Cell Metab.* **7,** 125–134
47. Stiles, B., Wang, Y., Stahl, A., Bassilian, S., Lee, W. P., Kim, Y. J., Sherwin, R., Devaskar, S., Lesche, R., Magnuson, M. A., and Wu, H. (2004) Liver-specific deletion of negative regulator Pten results in fatty liver and insulin hypersensitivity. *Proc. Natl. Acad. Sci. U.S.A.* **101,** 2082–2087
48. Brown, M. S., and Goldstein, J. L. (2008) Selective versus total insulin resistance: a pathogenic paradox. *Cell Metab.* **7,** 95–96
49. Benhamed, F., Denechaud, P. D., Lemoine, M., Robichon, C., Moldes, M., Bertrand-Michel, J., Ratziu, V., Serfaty, L., Housset, C., Capeau, J., Girard, J., Guillou, H., and Postic, C. (2012) The lipogenic transcription factor ChREBP dissociates hepatic steatosis from insulin resistance in mice and humans. *J. Clin. Invest.* **122,** 2176–2194
50. Beaven, S. W., Matveyenko, A., Wroblewski, K., Chao, L., Wilpitz, D., Hsu, T. W., Lentz, J., Drew, B., Hevener, A. L., and Tontonoz, P. (2013) Reciprocal regulation of hepatic and adipose lipogenesis by liver x receptors in obesity and insulin resistance. *Cell Metab.* **18,** 106–117
51. Zhou, Y., Abidi, P., Kim, A., Chen, W., Huang, T. T., Kraemer, F. B., Liu, J. (2007) Transcriptional activation of hepatic ACSL3 and ACSL5 by oncostatin M reduces hypertriglyceridemia through enhanced β-oxidation. *Arterioscler. Thromb. Vasc. Biol.* **27,** 2198–2205

The American Journal of Pathology, Vol. 184, No. 8, August 2014

ELSEVIER

The American Journal of
PATHOLOGY

ajp.amjpathol.org

GASTROINTESTINAL, HEPATOBILIARY, AND PANCREATIC PATHOLOGY

Semaphorin 3E Secreted by Damaged Hepatocytes Regulates the Sinusoidal Regeneration and Liver Fibrosis during Liver Regeneration

Tomoki Yagai,* Atsushi Miyajima,* and Minoru Tanaka[†‡]

From the Laboratories of Cell Growth and Differentiation and Stem Cell Regulation,[†] Institute of Molecular and Cellular Biosciences, The University of Tokyo, Tokyo; and the Department of Regenerative Medicine,[‡] Research Institute, National Center for Global Health and Medicine, Tokyo, Japan*

Accepted for publication
April 28, 2014.

Address correspondence to Minoru Tanaka, Ph.D., Laboratory of Stem Cell Regulation, Institute of Molecular and Cellular Biosciences, The University of Tokyo, 1-1-1 Yayoi, Bunkyo-ku, Tokyo 113-0032, Japan. E-mail: tanaka@iam.u-tokyo.ac.jp.

The liver has a remarkable capacity to regenerate after injury. Although the regulatory mechanisms of hepatocytic regeneration have been a subject of intense study, the dynamism of the sinusoids, specialized blood vessels in the liver, remains largely unknown. Transient activation of hepatic stellate cells and hepatic sinusoidal endothelial cells, which constitute the sinusoids, contributes to liver regeneration during acute injury, whereas their sustained activation causes liver fibrosis during chronic injury. We focused on understanding the association between damaged hepatocytes and sinusoidal regeneration or liver fibrogenesis using a carbon tetrachloride–induced liver injury mouse model. Damaged hepatocytes rapidly expressed semaphorin 3E (Sema3e), which induced contraction of sinusoidal endothelial cells and thereby contributed to activating hepatic stellate cells for wound healing. In addition, ectopic and consecutive expression of Sema3e in hepatocytes by the hydrodynamic tail-vein injection method resulted in disorganized regeneration of sinusoids and sustained activation of hepatic stellate cells. In contrast, liver fibrosis ameliorated in *Sema3e*-knockout mice compared with wild-type mice in a chronic liver injury model. Our results indicate that Sema3e, secreted by damaged hepatocytes, affects sinusoidal regeneration in a paracrine manner during liver regeneration, suggesting that Sema3e is a novel therapeutic target in liver fibrogenesis. *(Am J Pathol 2014, 184: 2250–2259; http://dx.doi.org/10.1016/j.ajpath.2014.04.018)*

The liver has a remarkable capacity to regenerate from surgical resection and damage caused by various insults, such as toxic chemicals and viral infection. Many injuries cause death of hepatocytes, which are liver parenchymal cells, followed by compensatory proliferation of the remaining hepatocytes to regenerate.[1] Therefore, the mechanisms of liver regeneration are focused on hepatocytes,[2,3] whereas the regenerative process of sinusoids, unique capillary vessels in the liver, remains largely unknown. The hepatic sinusoid is composed of fenestrated sinusoidal endothelial cells (SECs) and hepatic stellate cells (HSCs). In general, the process of liver regeneration after injury is accompanied by sinusoid fibrogenesis. Although transient fibrogenesis is beneficial for wound healing by providing mechanical stability and a scaffold for hepatocytic regeneration,[4] prolonged fibrogenesis during chronic hepatitis often leads to the accumulation of extracellular matrix (ECM), resulting in nodule formation and alterations in hepatic function and blood flow. Therefore, liver fibrosis is a pathologic sign that results in severe hepatic diseases, such as cirrhosis and carcinogenesis.[5] Previous studies have revealed that HSCs, characteristic pericytes that line the hepatic sinusoid, are a key cellular source for the ECM and that activated HSCs acquire myofibroblastic characteristics by secreting excess ECM protein, such as collagen types I and III.[6] In addition, SECs and HSCs cooperate to maintain the sinusoidal environment. For example, vascular endothelial growth factor (VEGF) secreted by HSCs maintains SEC homeostasis by preventing their capillarization.[7] Conversely, SECs revert activated HSCs to a

Supported in part by Grants-in-Aid for Scientific Research 22590719 and 22118006 from the Japan Society for the Promotion of Science, Japan (A.M. and M.T.).

Disclosures: None declared.

http://dx.doi.org/10.1016/j.ajpath.2014.04.018

quiescent status via nitric oxide synthesis.[8] These observations suggest that the reciprocal cell-to-cell communication between SECs and HSCs is critical for sinusoidal regeneration and liver fibrosis after liver injury and that SEC angiogenic factors could be the regulators of liver fibrogenesis through indirect activation of HSCs. Because liver injury is accompanied by inflammation and hepatocytic insults, inflammatory cells are involved in sinusoidal fibrogenesis.[9] In addition, molecules secreted from damaged hepatocytes contribute to the compensatory proliferation of surrounding hepatocytes.[10,11] However, whether there is a direct association between damaged hepatocytes and sinusoidal regeneration or liver fibrogenesis is currently unknown.

We found that semaphorin 3E (Sema3e) is up-regulated by 3,5-diethoxycarbonyl-1,4-dihydrocollidine feeding in a mouse model of chronic hepatitis.[12,13] Sema3e is a secretory protein that belongs to the class 3 semaphorin family[14] and plays a neurogenic and angiogenic repulsive role in development.[15,16] The receptors for semaphorins are plexins and neuropilins, and Sema3e specifically binds to plexin D1 (Plxnd1).[17] Sakurai et al[18] reported that Sema3e/Plxnd1 signaling initiates the antiangiogenic response by regulating Arf6 and R-Ras, inhibiting endothelial tip cell adhesion to the ECM, and retracting filopodia. Moreover, the Sema3e/Plxnd1 axis interferes with VEGF and VEGF receptor (VEGFR)-2 signaling via a feedback mechanism.[19] Indeed, Sema3e/Plxnd1 signaling plays an essential role in development because *Sema3e*-knockout (KO) mice display aberrant vascularization of intersomitic blood vessels.[17] However, the involvement of Sema3e/Plxnd1 signaling in liver regeneration and pathogenesis remains largely unknown. In this study, we focused on the mechanisms of sinusoidal regeneration after liver injury and found that Sema3e produced by damaged hepatocytes activates SECs via Plxnd1 and thereby plays a critical role in sinusoidal regeneration and liver fibrosis.

Materials and Methods

Mice

C57BL/6 mice were obtained from CLEA Japan (Tokyo, Japan). *Sema3e*-KO mice were provided by Dr. Yutaka Yoshida (Cincinnati Children's Hospital Medical Center, Cincinnati, OH).[17] The littermates were subjected to carbon tetrachloride (CCl_4)—induced liver fibrosis. All animal experiments were performed in accordance with our institutional guidelines.

Induction of CCl_4-Induced Acute Liver Injury and Liver Fibrosis

Acute liver injury was induced by single i.p. injection of CCl_4. CCl_4 (Wako Pure Chemical, Osaka, Japan) was diluted in corn oil (Wako) to 20% and injected into mice at a dose of 1 mL/kg of CCl_4. Liver fibrosis was induced by repeated injection of CCl_4, twice per week for 4 weeks. Livers were harvested 3 days after the final CCl_4 injection.

H&E and Sirius Red Staining

Liver cryosections (8 μm) were mounted on glass slides and fixed with Zamboni fixative solution for 10 minutes for immunostaining. The fixed sections were incubated with 5% skim milk (w/v) in phosphate-buffered saline and then incubated with primary antibodies, followed by secondary antibodies. The antibodies used in this study are listed in Table 1. Images were captured using Observer Z1 with an AxioCam HRc (Zeiss, Oberkochen, Germany). The hematoxylin and eosin (H&E) staining was performed after immunostaining in some specific experiments as stated later. The cover glass on enclosed sections was eliminated carefully with adequate phosphate-buffered saline (Wako) and then stained with H&E (Muto Pure Chemicals, Tokyo, Japan). Sirius Red staining was performed followed by Bouin's solution (Sigma-Aldrich, St. Louis, MO) fixation, as described previously. In brief, nuclei were stained with Weigert's iron hematoxylin (Wako) and then stained with collagen and Direct Red 80 (Sigma-Aldrich).

RT-PCR and Real-time RT-PCR

Total RNA was isolated from mouse livers or hepatic cells using TRIzol reagent (Invitrogen). Reverse transcription to cDNA templates was performed using random primers and a High-Capacity cDNA Reverse-Transcription Kit (Applied Biosystems, Foster City, CA). Real-time RT-PCR experiments were conducted with a LightCycler 480 system and Universal Probe Library (Roche Diagnostics, Indianapolis, IN). The mouse *ACTB* gene assay in ProbeLibrary was used as the normalization control. The sequence information for the primer pairs used is listed in Table 2. Probes #63 and #27 were used for *Sema3e* and *Plxnd1*, respectively. Sema3e primers were used for experiments by analyzing the Sema3e expression. Sema3e vector primers were used to construct the expression vector.

Table 1 Antibodies Used in the Study

Protein	Supplier
Semaphorin 3E (Sema3e)	Abgent (San Diego, CA)
Stabilin-2 (Stab-2)	Nonaka et al[20]
CD45	BD Biosciences (San Diego, CA)
Nerve growth factor receptor (NGFR, p75NTR)	R&D Systems (Minneapolis, MN)
Actin, α_2, smooth muscle, aorta (α-SMA)	Abcam (Cambridge, MA)
CD16/CD32 (Fcγ III/II Receptor)	BD Biosciences
Ki-67	eBioscience (San Diego, CA)
Collagen I	AbD Serotec (Kidlington, UK)
Phalloidin	Invitrogen (Carlsbad, CA)
GAPDH	Merck Millipore (Billerica, MA)

α-SMA, α-smooth muscle actin; GAPDH, glyceraldehyde-3-phosphate dehydrogenase; p75NTR, p75 low-affinity neurotrophic growth factor receptor.

Table 2 Primer Sequences Used for This Study

Gene	Sense primer sequence	Antisense primer sequence
Sema3e	5′-GGGGCAGATGTCCTTTTGA-3′	5′-AGTCCAGCAAACAGCTCATTC-3′
Plxnd1	5′-CTGGATGTCCATCTGCATGT-3′	5′-CAGGAAGAACGGCTCACCTA-3′
Construction for *Sema3e* expression vector	5′-AGCTAGCCCCTGGAGGGAAGTACTAA-3′	5′-GTCGACTCCTAGGTTCCTCAGCCGCC-3′

Cell Isolation

A single-cell suspension was obtained from the liver by a modified collagenase perfusion method, as described previously.[21] In brief, liver specimens were perfused with a basic perfusion solution containing 0.5 g/L of collagenase-Yakult (Yakult Pharmaceutical Industry Co. Ltd., Tokyo, Japan) and 50 mg/L of DNase I (Sigma-Aldrich). The digested liver was passed through a 70-μm cell strainer. After centrifugation at 60 × *g* for 1 minute, the precipitated cells were used as hepatocytes after Percoll (GE Healthcare, Piscataway, NJ) density centrifugation. The supernatant was transferred to a new tube and centrifuged at 120 × *g* for 2 minutes repeatedly until no pellet was visible. The final supernatant was centrifuged at 340 × *g* for 5 minutes, and the precipitated cells were used as non-parenchymal cells for cell isolation. Aliquots of cells were blocked with anti-FcγR antibody, co-stained with fluorescence- and/or biotin-conjugated antibodies, and then incubated with allophycocyanin-conjugated streptavidin (BD Biosciences, San Diego, CA) if needed. The samples were sorted by Moflo XDP (Beckman-Coulter, Fullerton, CA) or auto-MACS pro (Miltenyi Biotec, Bergisch Gladbach, Germany) with anti-allophycocyanin microbeads. Dead cells were excluded by propidium iodide staining.

Primary Culture of Hepatocytes and SECs

Primary hepatocytes separated by Percoll were seeded in type I collagen–coated 6-well dishes (BD Biosciences) at 5×10^5 per well with William's Medium E (Life Technologies, Carlsbad, CA) that contained 10% fetal bovine serum (JRH Biosciences, Lenexa, KS). After 3 hours (0 hours), unattached hepatocytes were washed out, and dimethyl sulfoxide (vehicle) or CCl_4 dissolved in dimethyl sulfoxide was added to the culture medium at a final concentration of 2.0 mmol/L. Then, total RNA was extracted from hepatocytes at 0, 3, 6, and 24 hours after CCl_4 administration. Isolated primary SECs were seeded in dishes coated with collagen type I-C (Nitta gelatin, Osaka, Japan) with Dulbecco's modified Eagle's medium/Ham's nutrient mixture F-12 (Sigma-Aldrich). After 12 hours, recombinant mouse Sema3e (R&D Systems) was added to the culture medium for a final concentration of 500 ng/mL. After incubation for 30 minutes, the morphologic status of SECs was analyzed by immunocytochemistry using fluorescein-conjugated phalloidin and Hoechst stain.

Forced Expression of Sema3e in Hepatocytes

We used the pLIVE vector and TransIT-EE Hydrodynamic Delivery solution (Mirus Bio, Madison, WI) to introduce Sema3e cDNA into 8-week-old mice by hydrodynamic tail-vein injection (HTVi). The primer pairs used for the expression vector are listed in Table 2.

Quantitative Analysis of Liver Sections Stained with Immunohistochemistry and Sirius Red

The vascular density was determined by analyzing stabilin (Stab)-2–positive area in the fields, including the central vein (CV). Four independent images of liver sections at ×200 magnification per animal were analyzed using the ImageJ software version 1.46r (NIH, Bethesda, MD). The parenchymal area was evaluated by subtracting vascular luminal area from the total field area and used for calculation. The fibrosis area was assessed by analyzing the Sirius Red–stained collagen areas in the liver sections at ×50 magnification. Ki-67–positive hepatocytes were counted using In Cell Analyzer 2000 (GE Healthcare), as described previously.[22]

Measurement of Serum ALT, Serum Albumin, and Hydroxyproline Content

Serum alanine aminotransferase (ALT) and albumin were measured at the Oriental Yeast Company (Tokyo, Japan) or by the Transaminase CII-test Wako (Wako). Hydroxyproline content was measured as described previously.[23]

Statistical Analysis

Statistical analysis was performed using the unpaired two-tailed Student's *t*-test. Gene expression in multiple liver cell fractions was compared by one-way analysis of variance and subsequent Tukey's tests. $P < 0.05$ was considered statistically significant.

Results

Sinusoidal Regeneration in CCl_4-Induced Liver Injury in Mice

The i.p. injection of CCl_4 produces a conventional liver injury model to study liver regeneration and subsequent fibrosis. We treated mice with CCl_4 and monitored the status of hepatocytes and SECs to investigate sinusoidal regeneration after liver injury. We have reported previously that Stab-2, a scavenger receptor, and receptors II (CD32) and III (CD16) for Fc fragment of IgG (FcγRs) are highly expressed in SECs and make it possible to distinguish SECs from other kinds of endothelial cells.[20,24] Frozen liver sections were subjected to immunohistochemistry (IHC) using

anti–Stab-2 or anti-FcγR antibodies, followed by H&E staining to visualize SECs in CCl_4-treated liver. Sinusoids in normal liver (0 hours) extended from the CV in a high-density radial pattern (Figure 1, A and B, and Supplemental Figure S1, A and B). Because CCl_4 is metabolized by cytochrome P450 in hepatocytes surrounding the CV to produce toxic free radicals as intermediate metabolites,[25] administering CCl_4 causes massive hepatocytic death around the CV. H&E staining revealed mild and obvious degeneration of hepatocytes at 24 and 48 hours after CCl_4 treatment, respectively (Figure 1, C and E, and Supplemental Figure S1, C and E). The sinusoidal structure was disorganized 24 hours after CCl_4 treatment, and most SECs in the degenerated region (Figure 1) seemed to be contracted, suggesting that some substantial alterations occurred in the SECs (Figure 1, C and D, and Supplemental Figure S1, C and D). The degenerated region became more obvious, and the arrangement of SECs remained disorganized 48 hours after CCl_4 treatment (Figure 1, E and F, and Supplemental Figure S1, E and F). Degeneration of hepatocytes decreased and hepatocytes regenerated 72 and 96 hours after CCl_4 treatment, but immune cells accumulated around the CV (Figure 1, G and I, and Supplemental Figure S1, G and I). In contrast, SECs returned to their original position and morphologic status during these phases (Figure 1, H and J, and Supplemental Figure S1, H and J). These data suggest that the process of sinusoidal regeneration would be completed by 72 hours after CCl_4-induced injury in mice.

Sema3e Is Expressed by Degenerating Hepatocytes during CCl_4-Induced Liver Injury

Because a sign of contraction was observed in SECs at 24 hours after CCl_4 treatment, it was supposed that some angiogenesis-related factors might be involved in this morphologic change. We found in our previous research about liver regeneration during chronic hepatitis that Sema3e is up-regulated in injured liver. Therefore, we examined the Sema3e expression pattern by quantitative RT-PCR (RT-qPCR) after CCl_4 treatment and measured serum concentrations of ALT as a liver injury marker (Figure 2, A and B). As a result, Sema3e expression was negligible in normal liver but was up-regulated drastically at 24 hours after CCl_4 treatment. Intriguingly, Sema3e expression then decreased sharply at 48 hours and returned to the basal level after 72 hours. These results suggest that up-regulation of Sema3e might be related with degeneration of hepatocytes, as evaluated by serum ALT (Figure 2, A and B), whereas rapid Sema3e down-regulation may represent completion of hepatocytic death. Therefore, we hypothesized that damaged hepatocytes could be a source for Sema3e. To address this hypothesis, we examined Sema3e expression in injured liver sections by IHC using an anti-Sema3e antibody. As expected, strong Sema3e signals were detected within the degenerating area around the CV 24 hours after CCl_4 treatment (Figure 2C). To investigate whether the cells expressing Sema3e were hepatocytes, we stimulated hepatocytes isolated from normal liver with CCl_4 in culture. Primary cultured hepatocytes became

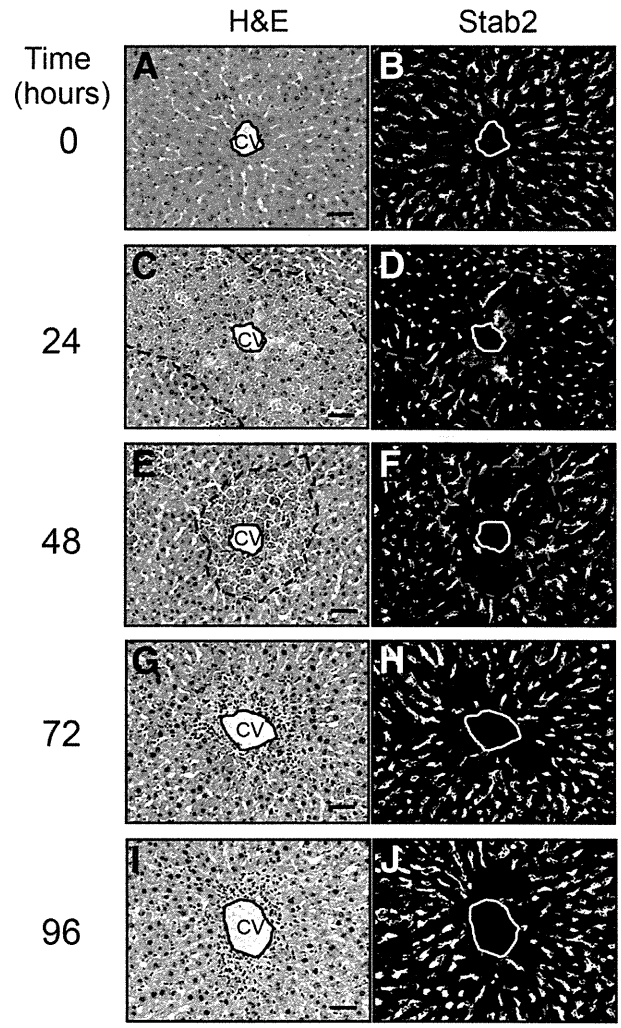

Figure 1 Morphologic transition of sinusoids after carbon tetrachloride (CCl_4)–induced liver injury. Identical sections were subjected to immunohistochemistry using anti-stabilin (Stab)-2 antibody and hematoxylin and eosin (H&E) staining (after immunostaining). **A** and **B:** The sinusoids extend from the central vein (CV) in a high-density radial pattern in normal liver (0 hours) before injury. **C** and **D:** Sinusoidal structure is affected 24 hours after CCl_4 treatment, followed by hepatocyte degeneration around the CV. **E** and **F:** Most sinusoidal endothelial cells (SECs) in the degenerated region (surrounded by the broken line) are strongly contracted. The arrangement of SECs remains disordered 48 hours after CCl_4 treatment. Degeneration of hepatocytes diminishes 72 (**G** and **H**) and 96 hours (**I** and **J**) after CCl_4 treatment, hepatocytes regenerate, and immune cells accumulate around the CV. Most of the SECs were stationed at the proper position during these phases. Scale bars: 50 μm (**A**, **C**, **E**, **G**, and **I**).

gradually swollen after CCl_4 treatment, and most of the hepatocytes degenerated 24 hours after CCl_4 challenge (Figure 2D). Real-time RT-PCR revealed that the expression level of Sema3e of CCl_4-treated hepatocytes was significantly increased compared with that of vehicle-treated or nontreated hepatocytes and 3.7-fold higher than that of injured liver 24 hours after *in vivo* administration of CCl_4 (whole liver), suggesting that damaged hepatocyte by oxidative stress is a major source of robust expression of Sema3e in CCl_4 injury model (Figure 2E). Although Sema3e is expressed in immune cells,[26] $CD45^+$ blood cells isolated from CCl_4-treated liver hardly expressed